



UNIVERSITY
of
GLASGOW

Department of Physics & Astronomy
Experimental Particle Physics Group

Kelvin Building, University of Glasgow,
Glasgow, G12 8QQ, Scotland

Telephone: +44 (0)141 339 8855 Fax: +44 (0)141 330 5881

GLAS-PPE/98-07

16th December 1998

Structure Functions

Anthony T. Doyle

Abstract

The latest structure function results, as presented at the ICHEP98 conference, are reviewed. A brief introduction to the formalism and the status of global analyses of parton distributions is given. The review focuses on three experimental areas: fixed-target results and their constraints on the parton densities at high x ; spin structure and spin parton densities as well as the status of the associated sum rules; HERA results on the dynamics of F_2 at low (x, Q^2) , charm and F_L as well as the measurement and interpretation of the high- Q^2 neutral and charged current cross-sections.

*Plenary talk presented at the XXIX ICHEP98 Conference,
Vancouver, July 1998.*

*Slides are available from
<http://www-zeus.desy.de/conferences98/#ichep98>*

arXiv:hep-ex/9812029v1 23 Dec 1998

1 Introduction - Formalism and Road Maps

The differential cross-section $l(k)N(p) \rightarrow l(k')X(p')$ for a lepton (e, μ) with four-momentum k scattering off a nucleon with four-momentum p can be expressed as

$$\frac{d^2\sigma(l^\pm N)}{dx dQ^2} = \frac{2\pi\alpha^2}{xQ^4} \cdot [Y_+ F_2(x, Q^2) \mp Y_- x F_3(x, Q^2) - y^2 F_L(x, Q^2)]$$

where Q^2 is the four-momentum transfer squared, $x = Q^2/2p \cdot q$ is the Bjorken scaling variable, $y = p \cdot q/p \cdot k$ is the inelasticity variable and $Y_\pm = 1 \pm (1 - y)^2$. The contribution from F_2 dominates the cross-section. The contribution from F_L is a QCD correction which is important only at large y and that from $x F_3$ is negligible for $Q^2 \ll M_Z^2$. To investigate sensitivity to F_L at large y or $x F_3$ at large Q^2 , the reduced cross-section $\tilde{\sigma} \equiv \frac{xQ^4}{2\pi\alpha^2} \frac{1}{Y_+} \frac{d^2\sigma}{dx dQ^2}$ is adopted. In the Quark Parton Model (or in the DIS scheme of NLO QCD) and for $Q^2 \ll M_Z^2$ F_2/x is the charge-weighted sum of the quark densities

$$F_2(x, Q^2) = x \sum_i e_i^2 \cdot \Sigma(x, Q^2)$$

where $\Sigma(x, Q^2) = \sum_i [q_i(x, Q^2) + \bar{q}_i(x, Q^2)]$ is the *singlet* summed quark and anti-quark distributions. Similarly, the charged current cross-section $e^+(e^-)N \rightarrow \nu(\bar{\nu})X$ at HERA can be expressed as

$$\frac{d^2\sigma^{CC}(l^\pm N)}{dx dQ^2} = \frac{G_F^2}{4\pi x} \left(\frac{M_W^2}{Q^2 + M_W^2} \right)^2 \cdot [Y_+ F_2^{CC}(x, Q^2) \mp Y_- x F_3^{CC}(x, Q^2)].$$

For fixed-target $\nu(\bar{\nu})N \rightarrow \mu^+(\mu^-)X$ experiments, $Q^2 \ll M_W^2$, and in the QPM

$$x F_3^{CC}(x, Q^2) = x \sum_i e_i^2 \cdot q_{NS}(x, Q^2)$$

where $q_{NS}(x, Q^2) = \sum_i [q_i(x, Q^2) - \bar{q}_i(x, Q^2)]$ is the *non-singlet* difference of these distributions.

In Fig. 1, the kinematic plane covered by the $F_2(x, Q^2)$ measurements is shown, including the new preliminary datasets from H1 and ZEUS which are seen to extend to: low y ($y_{\text{HERA}} \sim 0.005$) providing overlap with the fixed-target experiments; very low x ($x \lesssim 10^{-5}$) at low Q^2 exploring the transition region from soft to hard physics; high y ($y \rightarrow 0.82$) giving sensitivity to F_L ; high $x \rightarrow 0.65$ probing sensitivity to electroweak effects in F_2 and $x F_3$ as well as constraining the valence quarks at large Q^2 . The fixed-target experiments NMC, BCDMS, E665 and SLAC experiments have provided final measurements at higher x and lower Q^2 . New information was presented at ICHEP98 from CCFR, E866 and the Tevatron which also constrain the medium-high x partons.

Theoretically, the directions in (x, Q^2) can be mapped out according to the dominant dynamical effects, as illustrated in Fig. 2. Given a phenomenological input as a function of x , the parton

distributions are evolved to different physical scales (Q^2) via the DGLAP evolution equations. The alternative BFKL approach is to attempt to calculate the x dependence directly from pQCD, where the running of the effective coupling constant is neglected to leading order. BFKL predicts an $x^{-\lambda}$ dependence of F_2 at small x . The BFKL equation has recently been calculated to NLO. [1] These corrections are numerically very large in the experimentally accessible low (x, Q^2) range, resulting in $\lambda_{LO} \sim 0.5$ being reduced to $\lambda_{NLO} \sim 0.1$. The understanding of the NLO corrections to the BFKL equation is therefore an active area of study. [2] In the DLLA (‘double leading log approximation’), non-leading $\ln(Q^2) \ln(1/x)$ terms can also be evaluated, but a method which reliably maps the complete region of (x, Q^2) in terms of pQCD is still not known. The region of high parton density may be reached at very low x , where these approaches are not strictly valid. The expectation from the GLR equation [3] is that the region where the partons overlap is accessible at slightly higher x for decreasing Q^2 . However, Q^2 should also be sufficiently large that higher twist and non-perturbative effects parameterised in terms of Regge exchanges can be neglected.

In the DGLAP approach, the non-singlet contribution evolves as

$$\frac{\partial q_{NS}(x, Q^2)}{\partial t} = \frac{\alpha_s(Q^2)}{2\pi} P_{qq}^{NS} \otimes q_{NS}(x', Q^2)$$

where $t = \ln(Q^2/\Lambda^2)$ and the P_{ij} ’s represent the NLO DGLAP splitting probabilities for radiating a parton with momentum fraction x from a parton with higher momentum x' . Quantities such as xF_3 provide a measure of $\alpha_s(Q^2)$ which is insensitive to the a priori unknown gluon distribution. Similarly, the singlet quark and gluon densities are coupled via

$$\frac{\partial}{\partial t} \begin{pmatrix} \Sigma(x, Q^2) \\ g(x, Q^2) \end{pmatrix} = \frac{\alpha_s(Q^2)}{2\pi} \begin{bmatrix} P_{qq} & P_{qg} \\ P_{gq} & P_{gg} \end{bmatrix} \otimes \begin{pmatrix} \Sigma(x', Q^2) \\ g(x', Q^2) \end{pmatrix}$$

and quantities such as F_2 provide input for $\Sigma(x, Q^2)$ as well as coupled knowledge of $\alpha_s(Q^2)$ and the gluon, $g(x, Q^2)$.

At the starting scale, Q_o^2 , the light valence quarks (q_v) and the sea of quark and anti-quarks (\bar{q}) as well as the gluon (g) are attributed a given functional form. For example in the MRST parameterisations

$$f_i(x, Q_o^2) = A_i x^{\delta_i} (1-x)^{\eta_i} (1 + \epsilon_i \sqrt{x} + \gamma_i x)$$

where some parameters are set to 0 or fixed by sum rules and differences of u and d quarks may additionally be constrained. The heavy quark (sea) contributions are calculated explicitly at NLO and their uncertainty is typically determined by the range allowed for the effective mass of the heavy quark. The measured structure functions are then described by the convolutions of the light quark densities with the appropriate NLO matrix elements.

The outlined procedure defines the structure of a nucleon in terms of its constituent quarks and gluons. However, guided by the new datasets and analyses which were presented to this conference, it should be noted that the following assumptions are made:

- $\alpha_s(Q^2) \ln(Q^2)$ (DGLAP) terms are large compared to $\alpha_s(Q^2) \ln(1/x)$ (BFKL) terms in the perturbative splitting functions; ¹⁾

¹⁾ The study of inclusive quantities such as F_2 at small x are presently unable to distinguish these BFKL terms. The status of forward jet production searches which enhance sensitivity to these effects is reviewed by J. Huston. [4]

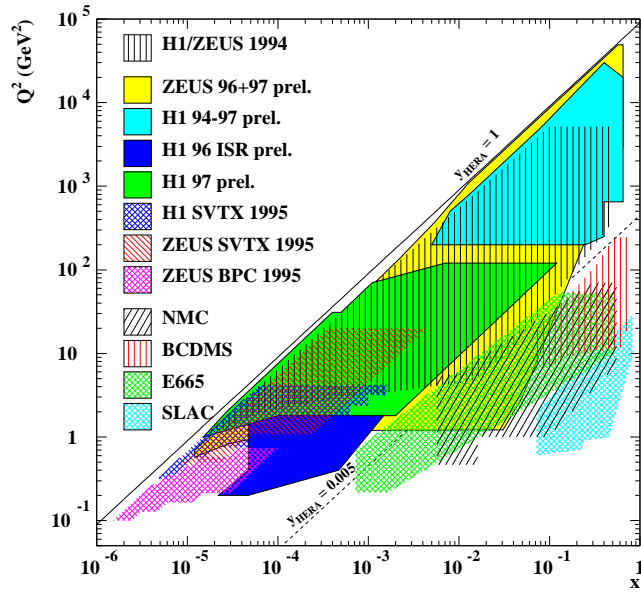


Figure 1: Measured regions of F_2 in the (x, Q^2) kinematic plane. The nominal acceptance region of the HERA measurements corresponds to $y_{\text{HERA}} > 0.005$. The fixed-target experimental data occupies the region of high x at low Q^2 .

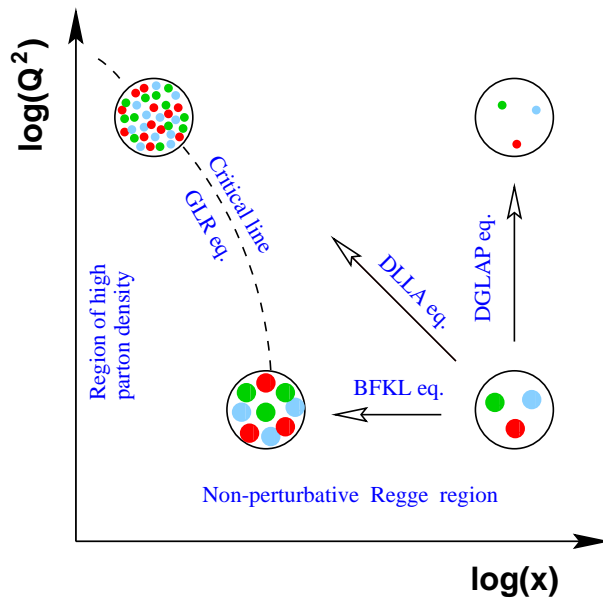


Figure 2: Schematic representation of parton densities and the theoretical evolution directions in the (x, Q^2) kinematic plane.

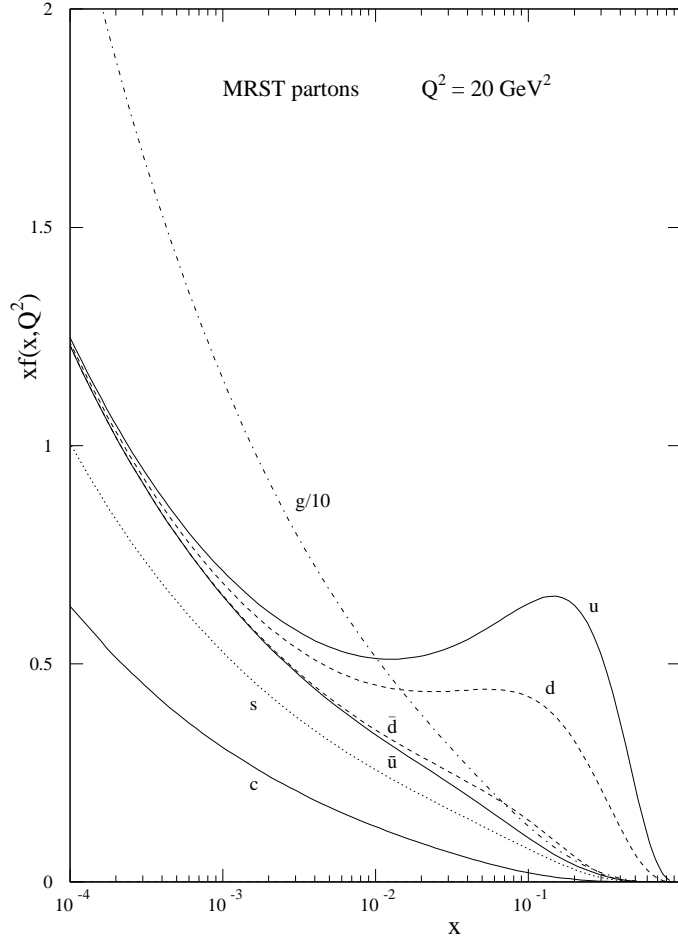


Figure 3: MRST parton distributions $xf(x, Q^2)$ at $Q^2 = 20 \text{ GeV}^2$.

- higher-twist (HT) contributions (suppressed by factors of $1/Q^2$) are negligibly small; ²⁾
- Nuclear binding effects are treated as small corrections or ignored in analyses of deuteron data. ³⁾

In Table 1, the experimental datasets considered in the MRST analysis are listed along with the underlying physics process and the parton behaviour which is being probed. The experiments denoted by † correspond to final measurements reported at ICHEP98. Those denoted by ★ correspond to new preliminary measurements reported at this conference. The latest global fits of MRST [7], GRV98 [8] and CTEQ4 [9] are used here to compare with the data.

The output MRST parton distributions evolved to $Q^2 = 20 \text{ GeV}^2$ are shown in Fig. 3. At this Q^2 , the expected fractions of the total momentum carried by the valence quarks is 25% (u_v) and

²⁾Progress in determining the size of these higher twist and other hadronisation power corrections via infra-red renormalons is reviewed by Y. Dokshitzer. [5]

³⁾A discussion of diffractive final states in D.I.S including nuclear effects is included in the review by M. Erdmann. [6]

10%(d_v), 6%($2\bar{u}$), 8%($2\bar{d}$), 5%($2s$) and 2%($2c$) is carried by the $q\bar{q}$ symmetric sea and 44%(g) is carried by the gluons.

Incorporating new datasets and theoretical understanding improves the precision with which individual parton densities are known. In particular, uncertainties in d/u at high x , \bar{d}/\bar{u} at intermediate x , s at all x values, g at low x and c at low x , are discussed in the context of the presentations made at ICHEP98.

2 Fixed-Target Results

2.1 Determination of α_s

Gross-Llewellyn Smith (GLS) Sum Rule: The GLS sum rule expresses the fact that there are three valence quarks in the nucleon, subject to QCD corrections

$$\int_0^1 xF_3(x, Q^2) \frac{dx}{x} = 3\left(1 - \frac{\alpha_s}{\pi} - a_2\left(\frac{\alpha_s}{\pi}\right)^2 - a_3\left(\frac{\alpha_s}{\pi}\right)^3\right) - \frac{\Delta HT}{Q^2}.$$

This is a fundamental prediction of QCD which, as a non-singlet quantity, is independent of the gluon distribution. The sum rule has been calculated to $\mathcal{O}(\alpha_s^3)$ and estimated to $\mathcal{O}(\alpha_s^4)$. [10, 11] The CCFR collaboration have now published their final results, [12] incorporating earlier neutrino measurements (WA25, WA59, SKAT, FNAL-E180 and BEBC-Gargamelle) to determine the GLS sum rule. In Fig. 4, the sum rule is proportional to the area under the data in four regions of Q^2 . The analysis of the world data enables $\alpha_s(3 \text{ GeV}^2)$ to be determined at NNLO ($\mathcal{O}(\alpha_s^3)$) accuracy and evolved to M_Z^2 as

$$\alpha_s(M_Z^2) = 0.114_{-0.006}^{+0.005}(\text{stat.})_{-0.009}^{+0.007}(\text{sys.})_{-0.005}^{+0.004}(\text{theory}).$$

The largest contribution to the systematic error is the uncertainty on the ratio of the total neutrino and anti-neutrino cross-sections, $\sigma_{\bar{\nu}}/\sigma_{\nu} = 0.499 \pm 0.007$ which determines the overall normalisation of xF_3 . This uncertainty will be improved with the NuTeV tagged ν - $\bar{\nu}$ beamline. The nuclear target corrections to the GLS sum rule are predicted to be small. [13] The largest theory uncertainty is that associated with the higher twist contribution, $\Delta HT = 0.15 \pm 0.15 \text{ GeV}^2$. Here, a renormalon approach, where chains of vacuum polarisation bubbles on a gluon propagator lead to a prediction of the higher twist contribution in the perturbative expansion, predicts a small correction, $\Delta HT < 0.02 \text{ GeV}^2$. Other models predict significantly larger HT corrections and the uncertainty encompasses this range. The renormalon approach is now rather successful in describing a range of power corrections to hadronic final state variables [5] and leads to a central value of $\alpha_s(M_Z^2) = 0.118$. The most recent analysis of the xF_3 data determines the same central value with a similar theoretical uncertainty. [14]

Scaling Violations at Large x : The most accurate method to determine $\alpha_s(M_Z^2)$ from the CCFR data remains the measurement of the scaling violations of the structure functions, F_2 and xF_3 , using a NLO QCD fit. [15] The scaling violation slopes $d(\log F_2)/d \log Q^2$ and $d(\log xF_3)/d \log Q^2$ are shown in Fig. 5. From F_2 , the high- x gluon is also constrained to be

$$xg(x, Q_0^2 = 5 \text{ GeV}^2) = (2.22 \pm 0.34) \times (1 - x)^{4.65 \pm 0.68}$$

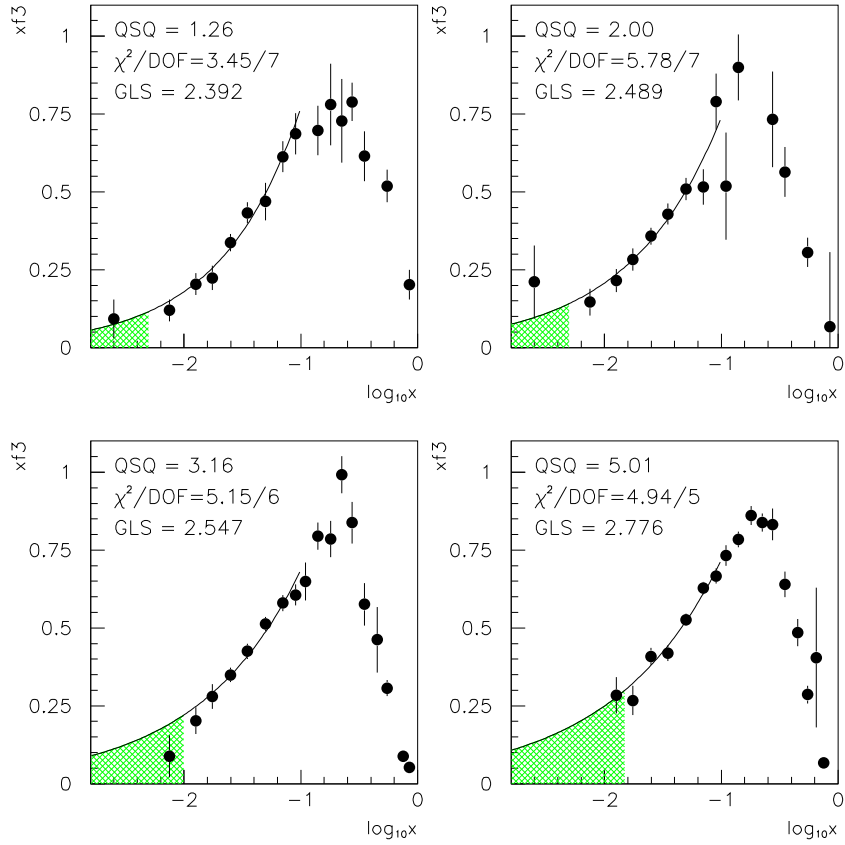


Figure 4: CCFR analysis of xF_3 versus $\log_{10}(x)$ for four ranges of Q^2 . The curve indicates a power law (Ax^B) fit applied for $x < 0.1$ used to determine the integral in the unmeasured shaded region.

in agreement with global analyses using prompt photon data. From the combined results on F_2 and xF_3

$$\alpha_s(M_Z^2) = 0.119 \pm 0.002(\text{exp.}) \pm 0.001(\text{HT}) \pm 0.004(\text{scale})$$

which represents one of the most precise determinations of this quantity. This improved measurement is higher than the earlier CCFR value due to the use of a new energy calibration. It is also higher than the SLAC/BCDMS analysis value of $\alpha_s(M_Z^2) = 0.113 \pm 0.003(\text{exp.}) \pm 0.004(\text{theory})$. [16] Here it is noted that there is a small but statistically significant discrepancy between the SLAC and BCDMS data (see the $x \geq 0.45$ F_2^p points in Fig. 6), which can be resolved if the correlated systematics of the BCDMS data at low y are taken into account. The quoted central value of the combined analysis, however, does not take these systematics into account. [18] There is therefore little evidence for any discrepancy with respect to the world average value $\alpha_s^{PDG}(M_Z^2) = 0.119 \pm 0.002$. [17]

Improved statistics will enable the NuTeV collaboration to determine α_s decoupled from the gluon using the xF_3 data alone. Further progress in the F_2 analysis requires the calculation of NNLO terms in order to reduce the renormalisation and factorisation scale uncertainties. In this way the overall uncertainty on $\alpha_s(M_Z^2)$ can be reduced to ± 0.002 . In this area, there is still an outstanding 20% discrepancy between the CCFR F_2^ν and NMC F_2^μ data in the region of $x \sim 10^{-2}$ which is discussed in the context of the strange quark sea and the ZEUS preliminary data later. However, this effect is negligible in the determination of α_s , which depends mainly upon the high- x data as seen in Fig. 5.

2.2 Nucleon Structure

d/u at large x: Valence parton distributions at high x received attention at this conference provoked by new data and corrections of the d/u ratio from an analysis by U. Yang and A. Bodek. [19] Extractions of F_2^n from NMC and SLAC deuteron data have previously accounted for Fermi motion but not nuclear binding effects. A physically appealing model by Frankfurt and Strikman [20] assumes that binding effects in the deuteron and heavier nuclear targets scale with the nuclear density. This nuclear binding correction is about 4% at $x = 0.7$ for fixed-target deuteron experiments, which is parameterised as an additional term $\delta(d/u) = (0.10 \pm 0.01)x(1+x)$ added to the MRS(R2) PDF. This is sufficient to increase the d distribution significantly at high $Q^2 = 10^4$ GeV² by about 40% at $x = 0.5$, due to DGLAP evolution of the partons. The modification gives an improved fit to the NMC deuteron data. It is compelling in that this simple modification now improves the description of high- x CDHSW $\nu p/\bar{\nu} p$ data (not shown) as well as the new data on the W asymmetry from CDF (probing intermediate $x \simeq M_W/\sqrt{s} \simeq 0.05$ values) and the charged current cross-sections from ZEUS (see later), data which are free from nuclear binding effects.

The world F_2^p and F_2^d fixed-target data at high x is plotted in Fig. 6. Here the NLO pQCD calculation incorporates target mass (TM) effects determined using Georgi-Politzer scaling where the scaling variable x is replaced by $\xi = 2x/(1 + \sqrt{1 + 4M^2x^2/Q^2})$ as well as the correction for nuclear binding effects for the deuteron data. The description of the low Q^2 data is significantly improved ($\chi^2/DoF = 1577/1045$) if higher twist (HT) corrections are incorporated as

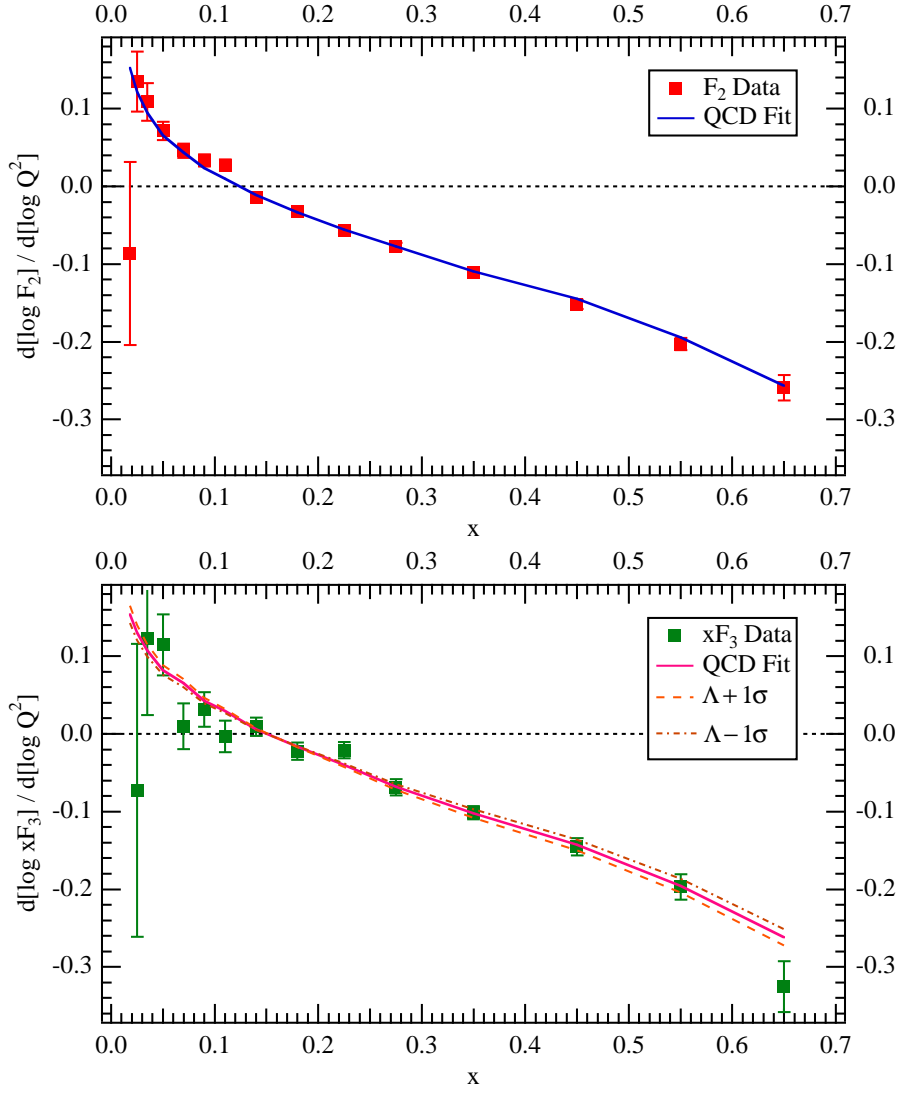


Figure 5: CCFR results on the scaling violations of F_2 (upper plot) and xF_3 (lower plot) compared to a NLO QCD fit.

indicated by the fit denoted NLO(pQCD+TM+HT). [19] A good description is also obtained for the very high x SLAC DIS data (not shown) up to $x = 0.9$, although there is some residual Q^2 dependence in the resonance region ($0.9 < x < 1$). The renormalon approach [21] therefore successfully predicts the x dependence of the higher twist terms although the normalisation constant is half of the previously estimated value. This renormalon approach also successfully describes the Q^2 dependence of $R = \sigma_L/\sigma_T$ (not shown). In a NNLO fit this higher twist contribution tends to zero which suggests that the non-singlet higher twist contribution (relevant for $x F_3$) is also small, as discussed in relation to the GLS sum rule. In addition, new measurements of R , covering the range of $0.015 < x < 0.55$ from CCFR were presented which are in agreement with those from EMC, BCDMS and SLAC and extend the kinematic range up to $Q^2 \sim 100 \text{ GeV}^2$. [22]

As can be seen in Fig. 3, the u quarks in the proton carry more momentum on average than the d quarks. (The \bar{d} quarks carry only slightly more momentum than the \bar{u} quarks at high x .) W^+ and W^- production in $\bar{p}p$ collisions is primarily due to the annihilation processes $u(p)\bar{d}(\bar{p}) \rightarrow W^+$ and $\bar{u}(\bar{p})d(p) \rightarrow W^-$. On average the W^+ 's are therefore produced relatively more forward than the W^- 's. CDF [23] measure the lepton asymmetry from the W decays,

$$A(y_l) = \frac{d\sigma^+/dy_l - d\sigma^-/dy_l}{d\sigma^+/dy_l + d\sigma^-/dy_l},$$

where $d\sigma^\pm/dy_l$ are the cross-sections for W^\pm decay leptons as a function of lepton rapidity relative to the proton beam direction. The W decay to leptons tends to reduce the asymmetry at forward $|y_l|$ but in a well-defined manner (assuming the W decays proceed via a SM $V-A$ interaction). In Fig. 7, the final results from runs Ia and Ib are shown compared to various PDF's using the DYRAD NLO calculations. The best agreement with the data is obtained using the modified MRS(R2) or the MRST PDF (not shown), which incorporates this data as input, indicating that the ratio of d/u is larger than previously thought.

\bar{d}/\bar{u} at intermediate x : The structure function measurements constrain the sum of \bar{d} and \bar{u} but not the difference. The classic method to constrain this difference is via the Gottfried sum rule where

$$S_G = \int_0^1 F_2^p - F_2^n \frac{dx}{x} = \frac{1}{3} \int_0^1 (d_v - u_v) dx - \frac{2}{3} \int_0^1 (\bar{d} - \bar{u}) dx.$$

The NMC result for $0.004 < x < 0.8$ extrapolated over all x gives $S_G = 0.235 \pm 0.026$, significantly below $1/3$. [24] It should be noted however that the deuterium data used to derive F_2^n are not corrected for the effects noted above. This correction is estimated to be -0.013 i.e. 50% of the uncertainty. [25]

At this conference, the E866 data were reported, [26] which provide a significant constraint on the ratio of \bar{d}/\bar{u} via the measurement of Drell-Yan dimuons with mass $M_{\mu^+\mu^-} \geq 4.5 \text{ GeV}$ from 800 GeV protons on proton and deuterium targets as shown in Fig. 8. Here, the ratio of $\sigma^{pd}/2\sigma^{pp}$ is measured as a function of the reconstructed momentum fraction of the target quark in the range $0.036 < x_2 < 0.312$. The MRST calculations incorporate a direct parameterisation of $\bar{d} - \bar{u}$ in order to fit the data. Earlier PDF's such as MRS(R2) clearly overestimate this asymmetry but a $\bar{d} = \bar{u}$ sea is still ruled out.

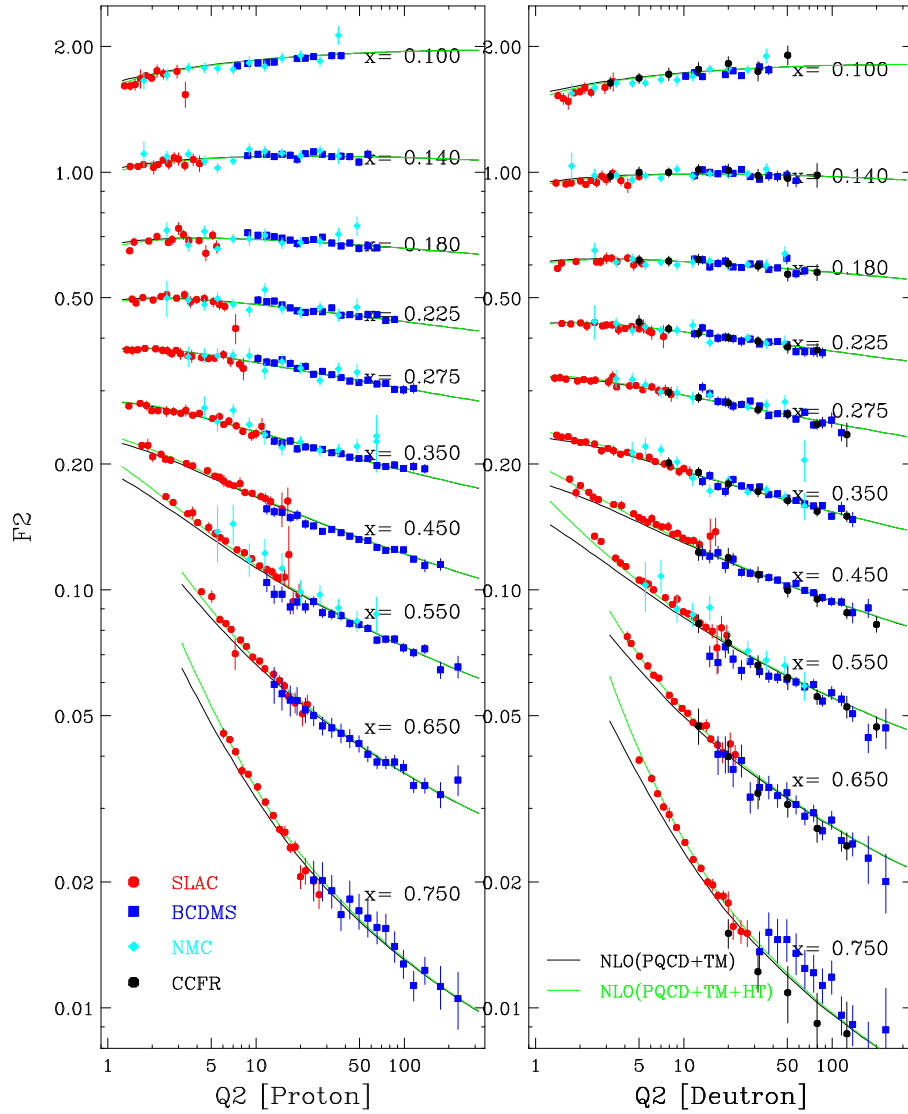


Figure 6: Comparison of high- x F_2^p and F_2^d data versus Q^2 fitted with and without higher twist (HT) corrections. The error bars correspond to statistical and systematic errors added in quadrature.

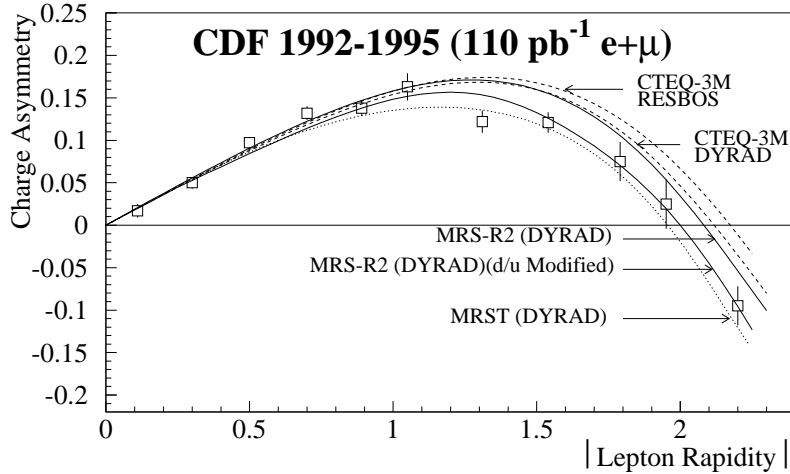


Figure 7: CDF lepton charge asymmetry from W decays as a function of lepton rapidity. The error bars correspond to statistical and systematic errors added in quadrature.

The E866 data require an overall decrease of the sea compared to the MRS(R2) parameterisation. This is seen in the lower part of Fig. 9 where the E866 data are plotted as the sea contribution to $F_2^p(x) - F_2^n(x)$, which contributes negatively to S_G , evolved to the NMC Q^2 values. The NMC data are plotted in the upper plot, compared to the valence as well as the summed contribution for the MRST and MRS(R2) partons. Although the valence and sea distributions differ, these distributions give similar results for the total $F_2^p(x) - F_2^n(x)$. However, it is clear that the agreement of the NMC data with either parameterisation is poor at intermediate x , which would require additional changes to the valence quark distributions. The MRST NLO fits determine $S_G = 0.266$, above the NMC measured value discussed earlier. This discrepancy is induced in part by the inclusion of the E866 data in the fit.

A further constraint is provided via the HERMES semi-inclusive measurement of the ratio of the differences between charged pion production for (unpolarised) proton and neutron (^3He) targets

$$r(x, z) = \frac{N_p^{\pi^-}(x, z) - N_n^{\pi^-}(x, z)}{N_p^{\pi^+}(x, z) - N_n^{\pi^+}(x, z)},$$

also reported at this conference. [28] The ratio is observed to scale as a function of the fragmentation scaling variable z and the data are used to constrain $(\bar{d} - \bar{u})/(u - d)$ at leading order as a function of x , as shown in Fig. 10a. Using the PDF's to constrain the valence quarks, the $\bar{d} - \bar{u}$ distribution obtained from the E866 and (lower Q^2) HERMES data are shown to be in agreement in Fig. 10b.

Generically, the Pauli exclusion principle, suppresses production of sea $u\bar{u}$ quarks at large x due to the additional u_v quark. Hence the excess of \bar{d} over \bar{u} is a direct consequence of the excess of u_v over d_v . The currently favoured dynamical approach is to include non-perturbative effects from virtual mesons directly from $|n\pi^+\rangle$ Fock states in a virtual pion model or to derive the

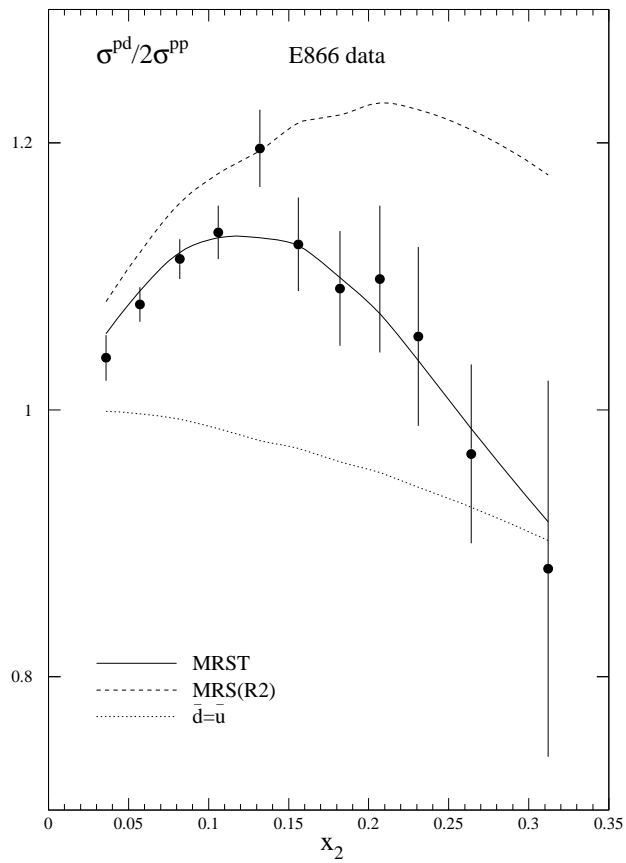


Figure 8: E866 ratio of $\sigma^{pp}/2\sigma^{pd}$ versus x_2 , the momentum fraction of the target quark, compared to the NLO calculations discussed in the text.

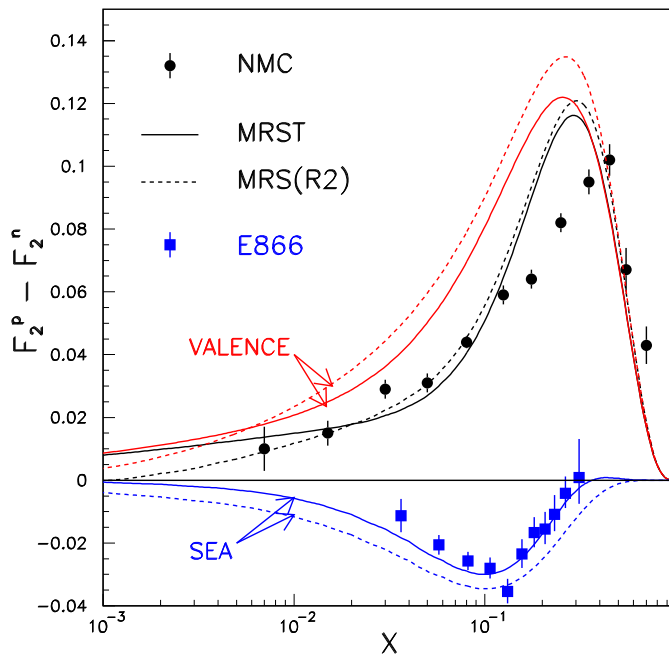


Figure 9: NMC $F_2^p - F_2^n$ versus x compared to LO predictions discussed in the text. For each prediction, the top (bottom) curve is the valence (sea) contribution and the middle curve is the sum. The E866 results for the sea quark contribution to $F_2^p - F_2^n$ are indicated as the negative contribution.

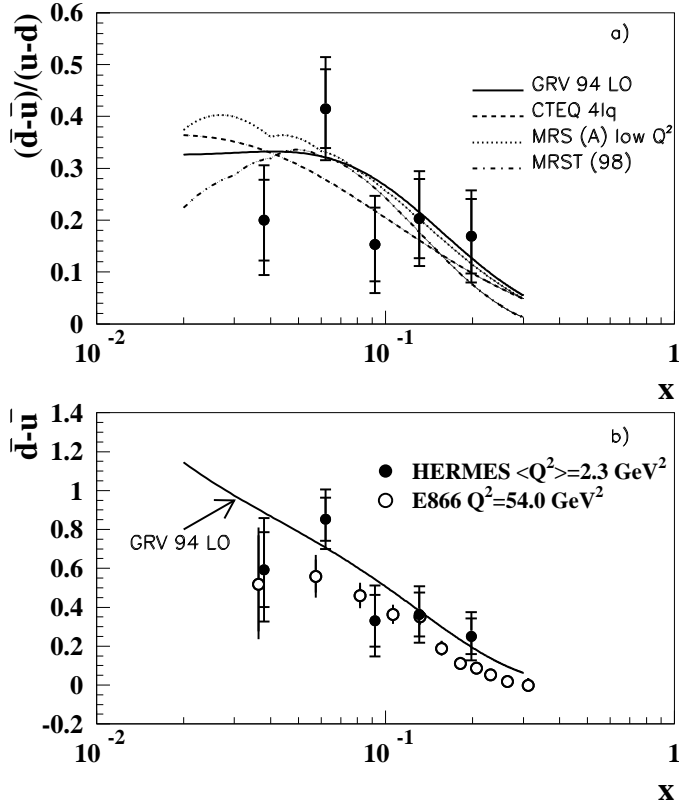


Figure 10: a) $(\bar{d} - \bar{u})(u - d)$ extracted directly from HERMES data (\bullet) compared to various parameterisations of the proton. b) HERMES data converted to $\bar{d} - \bar{u}$ in order to compare with E866 (\circ) data.

sea from the valence quarks coupling to Goldstone bosons (e.g. π^+ from $u \rightarrow d\pi^+$) in a chiral model. [27] In conclusion, the latest data indicate that the ratio of \bar{d}/\bar{u} is less than previously thought, a decrease which is correlated with the increase of d/u .

s quark contribution: The strange contribution to the quark sea is determined using opposite-sign dimuon events in νFe scattering from CCFR where one muon comes from the lepton vertex and the other results from the semi-leptonic decay of a charmed hadron. The ratio of s to u and d quarks integrated over x in an NLO analysis was determined to be $0.477^{+0.063}_{-0.053}$. [30] This large uncertainty requires, for example, that NuTeV tag ν and $\bar{\nu}$ and take the difference of these cross-sections in order to reduce the uncertainty on $\sin^2\theta_W$, also reviewed at this conference. [31] A second potential method to constrain the strange quark contribution is by comparing $F_2^{\nu N}$ and F_2^{lN} . The analysis of this data was discussed by C. Boros. [29] To leading order the muon (NMC) and neutrino (CCFR) structure functions are related by the “5/18ths rule”

$$F_2^{lN} = \frac{5}{18} \left[1 - \frac{3xs(x) + x\bar{s}(x)}{5xq(x) + x\bar{q}(x)} \right] F_2^{\nu N}$$

where the ($s\bar{s}$ symmetric) strange sea enters as a correction. However, the CCFR data corrected using the dimuon result to constrain the strange sea lies significantly ($\simeq 20\%$) above the NMC data for all values of Q^2 at $x < 0.1$. Here nuclear shadowing corrections, estimated independently for νFe (CCFR) and μD (NMC) data, indicate that part of the discrepancy between the two experiments at low x may be accounted for in this way. [29] However, there remains a significant discrepancy: the strange quark sea and the relation between $F_2^{\nu N}$ and F_2^{lN} data for $x < 0.1$ is therefore an active area of theoretical and experimental investigation.

3 Spin Structure Functions

Major progress has been made in the last two years in the measurement and QCD analysis of spin structure functions. The second generation CERN and SLAC experiments have been augmented by the HERMES experiment at DESY and these experiments now provide detailed information on the proton, neutron and deuteron spin structure. Here, we discuss measurements of the longitudinal asymmetry

$$A_{\parallel} = \frac{\sigma^{\downarrow\uparrow} - \sigma^{\uparrow\uparrow}}{\sigma^{\downarrow\uparrow} + \sigma^{\uparrow\uparrow}}$$

where $\sigma^{\uparrow\uparrow}$ ($\sigma^{\downarrow\uparrow}$) is the cross-section when the lepton and nucleon spins are parallel (antiparallel) to each other. This asymmetry takes into account the beam and target polarisations as well as the dilution factor, the fraction of polarisable nucleons in the target. The asymmetry can then be related to the virtual-photon nucleon asymmetries A_1 and A_2

$$A_{\parallel} = D(A_1 + \eta A_2)$$

where D is the depolarisation factor depending upon $R = \sigma_L/\sigma_T$ and $\eta = \eta(x, Q^2)$ is a kinematic factor. The spin structure function

$$g_1 = \frac{F_2}{2x(1+R)}(A_1 + \gamma A_2)$$

where γ is a further kinematic factor and g_1 is then calculated using the known F_2 and R values. The A_1 term dominates and to a reasonable approximation the extracted structure function is proportional to the measured asymmetry

$$g_1 \simeq \frac{F_2}{2x(1+R)} \cdot A_1 \simeq F_1 \cdot \frac{A_{\parallel}}{D}.$$

In the Quark Parton Model

$$g_1(x, Q^2) = \frac{1}{2} \sum_i e_i^2 \cdot \Delta\Sigma(x, Q^2)$$

where $\Delta\Sigma = \sum_i [(q_i^{\uparrow} - q_i^{\downarrow}) + (\bar{q}_i^{\uparrow} - \bar{q}_i^{\downarrow})]$ is the singlet summed quark and anti-quark distributions where q^{\uparrow} (q^{\downarrow}) is the quark distribution with the spins parallel (antiparallel) to the nucleon spin. In the QPM g_1 is therefore the charge-weighted vector sum of the quark polarisations in the

nucleon. Similarly the non-singlet quark distribution $\Delta q_{NS} = \sum_i \frac{e_i^2 - \langle e^2 \rangle}{\langle e^2 \rangle} [(q_i^\uparrow - q_i^\downarrow) + (\bar{q}_i^\uparrow - \bar{q}_i^\downarrow)]$, where $\langle e^2 \rangle = 2/9$ for 3 light flavours is defined such that this contribution evolves separately from the gluon (Δg) and singlet ($\Delta \Sigma$) contributions when QCD corrections are taken into account. The DGLAP formalism outlined earlier can therefore be applied and Δq_{NS} constrained by g_1 via QCD corrections.

The corresponding integrals $\Gamma_1 = \int_0^1 g_1(x, Q^2) dx$ determine the total spin carried by the quarks at the measured Q^2 . In the QPM, below charm threshold

$$\Gamma_1^p = \frac{1}{2} \left(\frac{4}{9} \Delta u + \frac{1}{9} \Delta d + \frac{1}{9} \Delta s \right)$$

and, by isospin symmetry

$$\Gamma_1^n = \frac{1}{2} \left(\frac{1}{9} \Delta u + \frac{4}{9} \Delta d + \frac{1}{9} \Delta s \right)$$

Beyond the QPM, the total spin of the nucleon can be written as the sum of the contributions from its constituents

$$\frac{1}{2} = \frac{1}{2} \Delta \Sigma + \Delta g + L_q + L_g$$

where the Δ 's correspond to the intrinsic spins and the L 's correspond to the angular momentum of the quarks and gluons. The proton spin puzzle is that only a fraction of the total spin is due to quarks. This puzzle remains, but first steps have now been taken to constrain the gluon contribution via the scaling violations of $g_1(x)$ and the valence and sea quark contributions via semi-inclusive measurements.

The world data on $g_1(x)$ for the proton, deuteron and neutron are summarised in Fig. 11 for the CERN, SLAC and DESY experiments. [32] Comparison of the lower and higher Q^2 data indicates that the scaling violations are relatively small over the well-measured range of $1 < Q^2 \lesssim 10 \text{ GeV}^2$. The data are taken using a variety of targets (e.g. H(p), D(d) and $^3\text{He}(n)$ for HERMES; NH₃(p), ND₃(d), $^6\text{LiD}(d)$ and $^3\text{He}(n)$ for the SLAC experiments; and, NH₃(p), butanol(p) and deuterated-butanol(d) for SMC) and widely varying experimental techniques.

There is no evidence for a rise of g_1^p at the smallest values of $x \sim 10^{-2}$ explored by SMC and E155. Indeed the QCD fit prediction is that g_1^p becomes negative for $x \lesssim 10^{-3}$ due to the relatively large positively polarised gluon at higher x driving the polarised gluon negative at small x . [33] Clearly this will be of interest in the light of the HERA unpolarised results and of significance in the extrapolations required for the determination of the sum rules. SMC presented data on the virtual-photon proton asymmetry, A_1^p at low $\langle Q^2 \rangle = 0.01 \text{ GeV}^2$ which extend to very low $x = 10^{-4}$, as shown in Fig. 12. [35] The low x data were obtained with a dedicated low- Q^2 trigger, requiring an observed hadron in each event which rejects radiative and other events with low depolarisation factors. At these very low Q^2 values the data indicate that extreme QCD behaviour of $g_1^p \propto 1/x \ln^2 x$ (full line) proposed in [36] is ruled out. However the less extreme QCD behaviours $g_1^p \propto \ln x$ or $2 + \ln x$ indicated by the dotted lines give reasonable descriptions of the data. Clearly higher Q^2 data are desirable in order to test the pQCD models, but the data do constrain the Regge behaviour.

The values of g_1^n in Fig. 11 fall monotonically with decreasing x . The precision of this data is now approaching that of the proton data, which is important in the context of the Bjorken

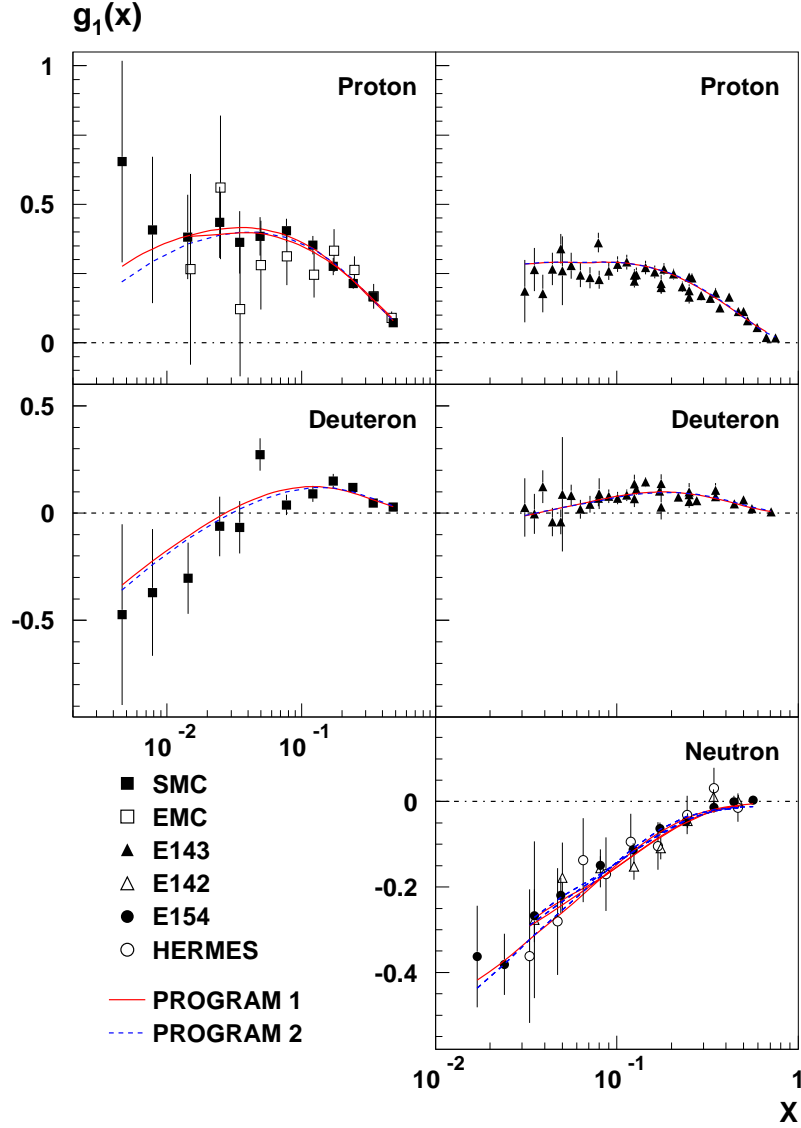


Figure 11: Published world data on $g_1(x)$ from CERN experiments ($0.003 < x < 0.6$, $1 < Q^2 < 100 \text{ GeV}^2$) in the left column and SLAC and DESY experiments ($0.014 < x < 0.7$, $1 < Q^2 < 20 \text{ GeV}^2$) in the right column with statistical errors only. Results from two ($\overline{\text{MS}}$ scheme) NLO QCD fitting programs discussed in the text are superimposed.

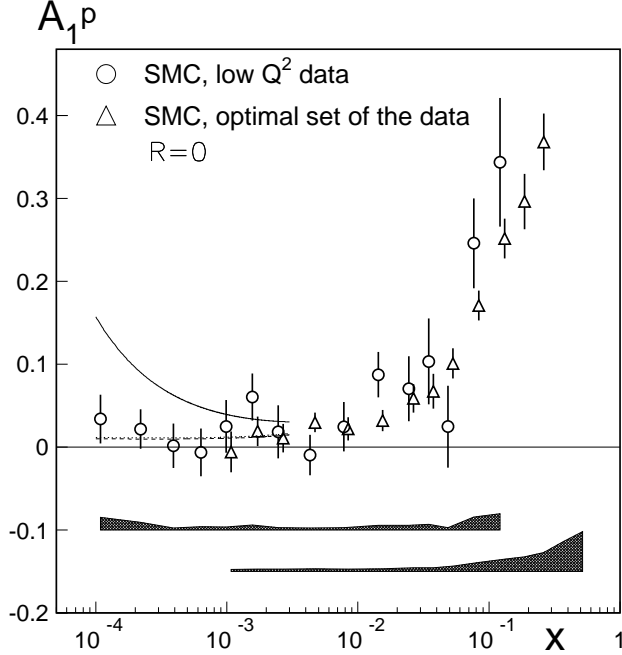


Figure 12: SMC virtual-photon proton asymmetry, A_1^p , for $\langle Q^2 \rangle \leq 0.01 \text{ GeV}^2$ data as a function of x compared to the behaviours discussed in the text. The systematic errors for the low (x, Q^2) and the reference set of data are indicated by the shaded bands.

sum rule discussed below. All data are observed to be in good agreement, where the systematic errors (not shown) are typically smaller than the statistical errors. In addition, E155 presented new preliminary data on g_1^p and g_1^n (not shown) at $Q^2 = 5 \text{ GeV}^2$ which are in good agreement with these published datasets. [34] These data have very small statistical errors and extend the x range compared to the E143 data. This improved precision also requires that nuclear effects due to the assumed superposition of D and ^4He states in the ^6Li target data are understood, but possible uncertainties can be tested by comparison with data from different targets and other experiments.

SMC have performed a NLO QCD fit [32] to extract the singlet $(x \cdot \Delta\Sigma)$ and gluon $(x \cdot \Delta g)$ as well as the proton $(x \cdot \Delta q_{NS}^p)$ and neutron $(x \cdot \Delta q_{NS}^n)$ non-singlet polarised parton distributions shown in Fig. 13. Here, the deuteron spin structure function g_1^d is assumed to be related to the proton and neutron structure functions by

$$g_1^p + g_1^n = \frac{2g_1^d}{1 - \frac{3}{2}\omega_D}$$

where $\omega_D = 0.05 \pm 0.01$ is the D-wave state probability in the deuteron.

The results of the fits from two NLO QCD programs are shown by the full and dashed lines in Fig. 11 at the measured Q^2 of each of the datasets. The comparison indicates that a good fit is obtained to the world data with $\chi^2/DoF = 127.4/(133 - 8)$, considering statistical errors only.

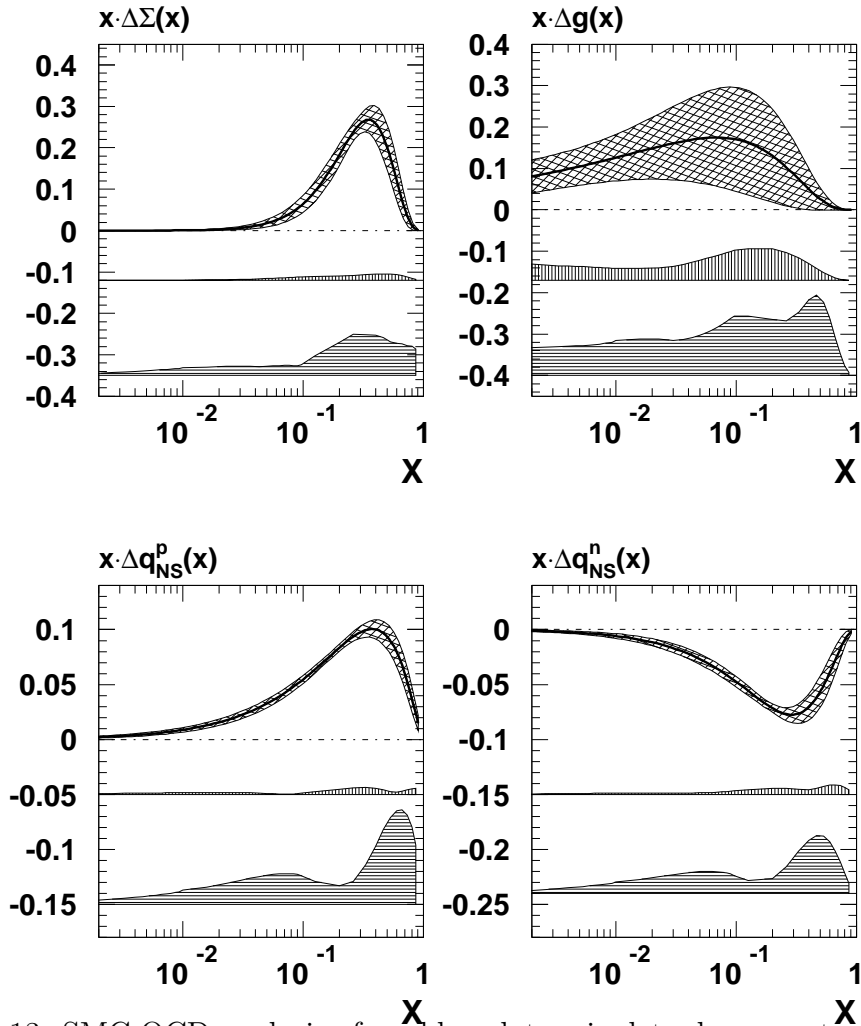


Figure 13: SMC QCD analysis of world g_1 data: singlet, gluon, proton and neutron non-singlet polarised parton distributions in AB scheme at $Q_0^2 = 1 \text{ GeV}^2$. The fits with the statistical uncertainty are indicated by the cross hatched upper bands. The (small) experimental systematic uncertainties are indicated by the central bands and the (larger) theoretical uncertainties by the lower bands.

The parton densities are parameterised and determined in analogy to the unpolarised case via the NLO DGLAP splitting kernels. Results are quoted in the Adler-Bardeen (AB) scheme, a modified version of the more conventional $\overline{\text{MS}}$ scheme, defined such that $\Delta\Sigma_{\text{AB}}$ is independent of Q^2 . These renormalisation/factorisation schemes are related via

$$\begin{aligned}
 a_0(Q^2) &= \Delta\Sigma_{\overline{\text{MS}}}(Q^2) \\
 &= \Delta\Sigma_{\text{AB}} - n_f \frac{\alpha_s(Q^2)}{2\pi} \Delta g_{\text{AB}}(Q^2)
 \end{aligned}$$

where $a_0(Q^2)$ is the singlet axial-current matrix element and the Δ 's correspond to the parton densities integrated over x . This scheme dependence is large and sufficient to create a negative $\Delta\Sigma(x)$ at small x and a smaller $\Delta g(x)$ in $\overline{\text{MS}}$ scheme. [32] However, the physical structure

functions and their integrals, such as $a_0(Q^2)$ are unaffected by this definition. In Fig. 13, the singlet contribution is seen to be well constrained by g_1^p . This remains true when account is taken of the theoretical uncertainties which include the variation of the renormalisation and factorisation scale by factors of two, varying $\alpha_s = 0.118 \pm 0.003$ within the given limits and changes to the starting scale and the functional forms of the parameters. Similarly the non-singlet contributions are reasonably well constrained and the rise of Δq_{NS}^p is mirrored by the fall of Δq_{NS}^n . However, Δg is rather poorly constrained especially when taking into account the theoretical uncertainties. Integrating over x at $Q_0^2 = 1 \text{ GeV}^2$

$$\Delta g = 0.99_{-0.31}^{+1.17}(\text{stat.})_{-0.22}^{+0.42}(\text{sys.})_{-0.45}^{+1.43}(\text{theory})$$

in AB scheme compared to $\Delta g = 0.25_{-0.22}^{+0.29}(\text{stat.})$ in $\overline{\text{MS}}$ scheme. Consistent results are obtained in either scheme for the singlet contribution expressed in terms of the axial-current matrix element

$$a_0(Q_0^2 = 1 \text{ GeV}^2) = 0.23 \pm 0.07(\text{stat.}) \pm 0.19(\text{sys.})$$

which compares to the QPM expectation $\simeq 0.58$ and corresponds to about one third of the nucleon spin being carried by quarks.

In the latest analysis by J. Ellis and M. Karliner, [37] the world average value of the singlet matrix element in $\overline{\text{MS}}$ scheme is given by

$$\Delta\Sigma = 0.27 \pm 0.05.$$

This approach utilises the $\mathcal{O}(\alpha_s^3)$ calculations and $\mathcal{O}(\alpha_s^4)$ estimates discussed below in relation to the Bjorken sum rule. Here, the consistency of the data taken at different Q^2 values improves as successive higher-order QCD corrections are taken into account.

Bjorken Sum Rule: The Bjorken sum rule is a fundamental prediction of QCD determined by the difference of the spins carried by the u and the d quarks

$$\Gamma_1^p - \Gamma_1^n = \int_0^1 (g_1^p - g_1^n) dx = \frac{1}{6} \left| \frac{g_A}{g_V} \right| \cdot C_1^{NS}(Q^2)$$

where g_A and g_V are the axial-vector and vector weak coupling constants of neutron β -decay and $C_1^{NS}(Q^2)$ is the non-singlet perturbative QCD correction which has been calculated up to $\mathcal{O}(\alpha_s^3)$ and estimated up to $\mathcal{O}(\alpha_s^4)$ using the same approach as for the GLS sum rule. [10, 11] Here, higher twist contributions to the difference of the structure functions are assumed to be negligibly small.

In the SMC NLO fits discussed above, the sum rule is imposed as an input with $|\frac{g_A}{g_V}|$ fixed rather precisely from β -decay experiments. However, the NLO fits provide two methods to check the Bjorken sum rule. First, the input can be relaxed and $|\frac{g_A}{g_V}|$ fitted as an additional parameter in the global fit yielding

$$\Gamma_1^p - \Gamma_1^n = 0.174 \pm 0.005(\text{stat.})_{-0.009}^{+0.011}(\text{sys.})_{-0.006}^{+0.021}(\text{theory})$$

at $Q^2 = 5 \text{ GeV}^2$, which is in agreement with the theoretically expected value of 0.181 ± 0.003 . Second, the non-singlet contributions $g_1^p - g_1^n$ can be evolved to a common Q^2 in order

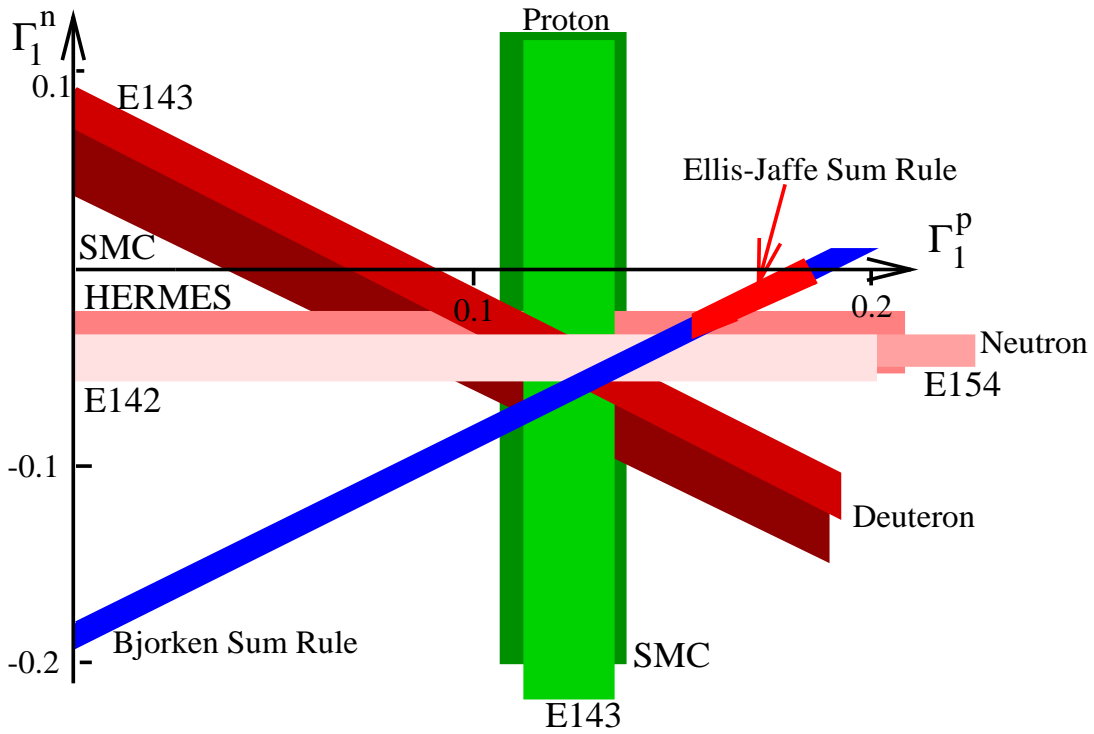


Figure 14: Spin sum rules Γ_1^p versus Γ_1^n . Proton (E143 and SMC) and neutron (E142, E154 and HERMES) data are indicated by the vertical and horizontal bands, respectively. Deuteron (E143 and SMC) data are indicated by the falling diagonal bands. The theoretical expectation from the Bjorken sum rule ($= \Gamma_1^p - \Gamma_1^n$) is indicated by the rising diagonal band while the Ellis-Jaffe sum rule is the area on this band indicated by the arrow.

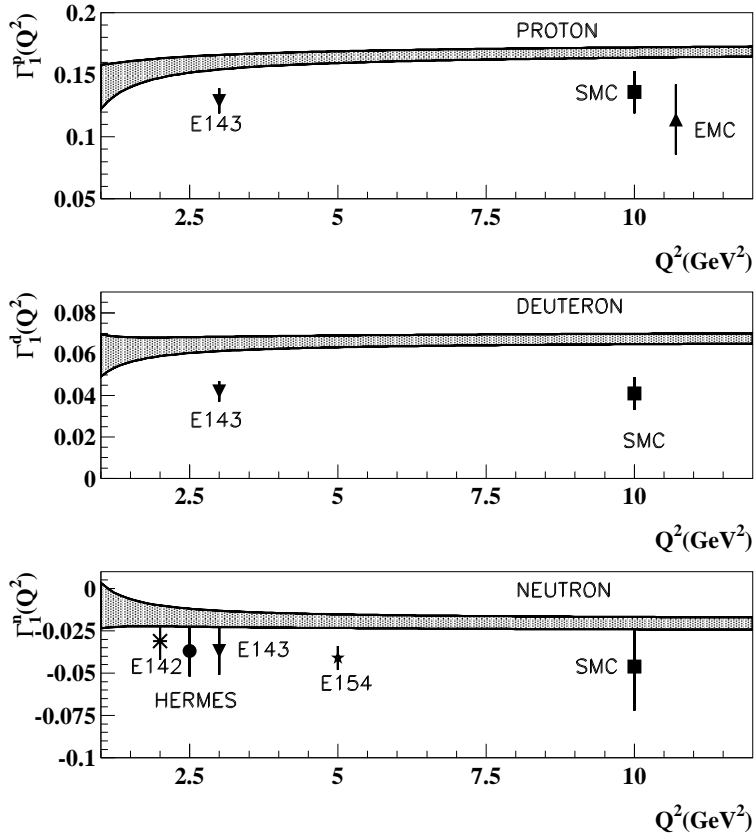


Figure 15: Spin integrals, Γ_1 proton, deuteron and neutron data versus Q^2 compared to the Ellis-Jaffe sum rule ($\Delta s = 0$ and $SU(3)_f$ symmetry) expectation indicated by the shaded band.

to determine the sum rule more directly and with a minimum number of parameters. This yields a consistent value of $0.181_{-0.021}^{+0.026}$ (*total*) when evaluated at $\mathcal{O}(\alpha_s^2)$. This second method is potentially more precise, but awaits the high statistics data on g_1^p from E155 combined with the existing data on g_1^n from E154.

Ellis-Jaffe Sum Rule: Assuming that strange quarks do not contribute to the nucleon spin and $SU(3)_f$ symmetry, Ellis and Jaffe derived independent sum rules for the proton and neutron

$$\Gamma_1^p = \frac{1}{2} \left(\frac{4}{9} \Delta u + \frac{1}{9} \Delta d \right) \simeq 0.17$$

$$\Gamma_1^n = \frac{1}{2} \left(\frac{1}{9} \Delta u + \frac{4}{9} \Delta d \right) \simeq -0.02$$

in the high- Q^2 limit and modified by singlet and non-singlet QCD corrections. In Fig. 14 the world data on the Bjorken and Ellis-Jaffe sum rules are depicted graphically. As noted in relation to the SMC analysis, the data are in agreement and consistent with the Bjorken sum rule with a precision of around 10%. The origin of the spin puzzle was the EMC measurement of Γ_1^p . In Fig. 15, the world data on Γ_1^p , Γ_1^d and Γ_1^n all indicate that the Ellis-Jaffe sum rule is broken at the 2-3 σ level. The strange sea quarks and/or the gluon therefore carry a significant fraction of the spin. It is currently impossible to distinguish an $SU(3)_f$ symmetric sea or a $\Delta s = 0$ (large gluon) solution in the NLO QCD fits. [38] A natural assumption would be that $SU(3)_f$ symmetry is violated at the same level as in the unpolarised structure functions and the rest of the spin can be attributed to a large gluon polarisation, but this requires further experimental input.

Semi-inclusive Asymmetries: SMC [39] and HERMES [40] have recently produced data tagging the charge of final state hadrons. The asymmetry $A_{||}^h(x, z)$ is defined in analogy to the inclusive case where the distribution of charged hadrons with momentum fraction z is statistically correlated with the struck quark flavour in a flavour tagging analysis. In Fig. 16 the extracted spin contributions Δu_v , Δd_v and $\Delta \bar{q}$ (introduced for $x < 0.3$) from SMC and HERMES are observed to be in agreement. Slightly different assumptions are made with respect to the strange quark sea where SMC assume an $SU(3)_f$ symmetric sea and HERMES assume this symmetry is violated at the same level as in the unpolarised structure functions. However these effects are negligible for the predominantly pion final states in this LO QCD analysis. Both experiments observe Δu_v is positive and Δd_v is negative. The SMC results integrated over x are

$$\Delta u_v = +0.77 \pm 0.10(\text{stat.}) \pm 0.08(\text{sys.})$$

$$\Delta d_v = -0.52 \pm 0.14(\text{stat.}) \pm 0.09(\text{sys.})$$

$$\Delta \bar{q} = +0.01 \pm 0.04(\text{stat.}) \pm 0.03(\text{sys.})$$

in agreement with the expectations from the NLO QCD fits. The polarised sea is compatible with zero although there are indications from the HERMES data that this contributes positively.

Outlook: The analysis of polarised structure function data enables first measurements of the scaling violations to be performed. These provide a test of QCD and indicate that the gluon polarisation is positive. Similarly, the semi-inclusive measurements give first constraints on

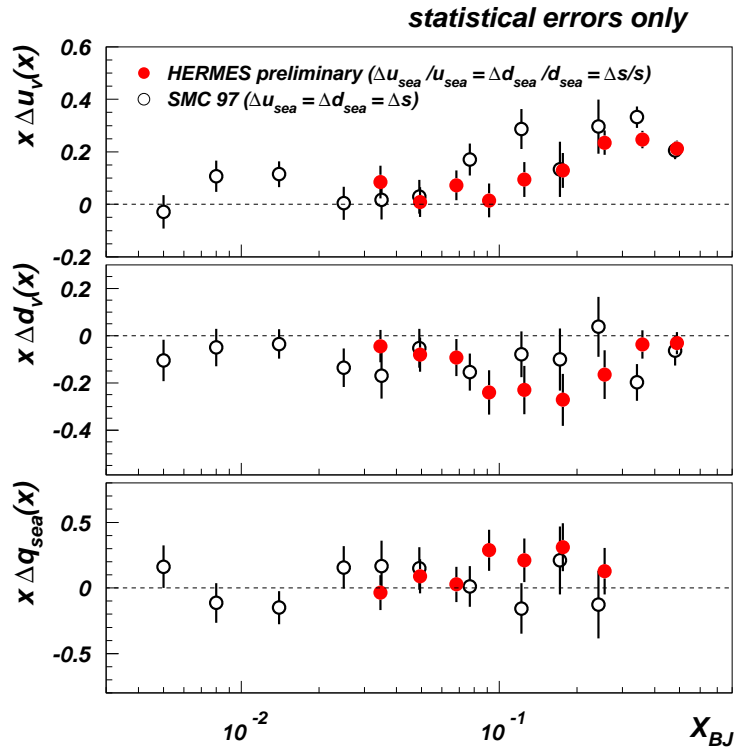


Figure 16: Data from SMC and HERMES for the valence (Δu_v and Δd_v) and sea ($\Delta \bar{q}$) spin densities versus x extracted from semi-inclusive asymmetry measurements. The dominant statistical errors only are shown.

the sea. The structure function data from E155 and semi-inclusive data from HERMES will soon provide further input. These data are, however, insufficient to determine the various spin parton distributions within the nucleon. By analogy with Table 1, we can therefore consider a future programme of spin structure measurements which will enable the partonic spin structure to be unravelled, as shown in Table 2. In the next few years HERMES, COMPASS and the RHIC experiments will focus on the determination of the gluon. It is also possible that the polarised proton technology developed at RHIC could be utilised at HERA in order to explore polarised structure functions at low (x, Q^2) . With a high luminosity HERA machine the data would also extend to high Q^2 where neutral current and charged current events would provide detailed information on this spin structure.

4 HERA Results

The HERA ep collider has improved its performance in successive years, providing large e^+p datasets from 1994-97 running. During this period 27.5 GeV positrons collided with 820 GeV protons resulting in data samples of 37pb^{-1} and 46pb^{-1} for H1 and ZEUS, respectively. As a measure of the progress which has been made in the study of the scaling violations of F_2 , Fig. 17 illustrates how the latest HERA data, presented for the first time at ICHEP98, extend the reach in Q^2 beyond $10,000\text{ GeV}^2$ with x extending up to 0.65. At high Q^2 values, the effects of Z^0 exchange are significant and the value of F_2^{em} is quoted where

$$F_2 = F_2^{em} + \frac{Q^2}{Q^2 + M_Z^2} F_2^{int} + \left(\frac{Q^2}{Q^2 + M_Z^2} \right)^2 F_2^{wk}$$

where F_2^{em} , F_2^{int} and F_2^{wk} are the contributions due to photon exchange, γZ interference and Z exchange, respectively. The data also extend to very low x below 10^{-5} : here it should be noted that the precision of the low- $x \lesssim 0.03$ data is now comparable to that of the fixed-target data at higher x . There is a region of overlap where the HERA and fixed-target experiments can be compared. In particular, the analysis of the ZEUS results at low y may resolve the CCFR-NMC discrepancy discussed earlier in the context of the “5/18ths rule”. However, this comparison (not shown) is currently inconclusive, with the ZEUS data lying between the NMC and CCFR data.

4.1 Low- Q^2 Results

Transition Region: The rise of F_2 with decreasing x or, equivalently, the rise of $\sigma_{\gamma^*p}^{tot}$ with increasing W has stimulated significant experimental and theoretical developments in the understanding of QCD at high energies. One challenge is to explore how and where the transition occurs from soft to hard physics and interpret low- Q^2 data. Measurements have been performed using dedicated low-angle taggers (e.g. the ZEUS BPC) and shifted vertex (SVX) data [41] as well as QED Initial State Radiation (ISR) data [42] in order to map out this region. In Fig. 18, a compilation of the latest measurements available from HERA and E665 indicates that the different experiments and techniques agree with a precision of around 5% from the most recent

data. The significant rise of F_2 is apparent for $Q^2 \gtrsim 1 \text{ GeV}^2$, a behaviour which is described by the ZEUS NLO (pQCD) fit. This behaviour is not reproduced in the DL (Donnachie-Landshoff Regge) fit. The ZEUS collaboration has performed both types of fits to the F_2 data exploring this transition region. [41] In order to determine the relationship between low- Q^2 ZEUS BPC data measured in the range $0.1 < Q^2 < 0.65 \text{ GeV}^2$ and $Q^2 = 0 \text{ GeV}^2$ data, a Generalised Vector Meson Dominance (GVMD) approach can be taken. GVMD relates the virtual-photon cross-section to the real cross-section via

$$\sigma_{\gamma^*p}^{\text{tot}} = \sigma_{\gamma p}^{\text{tot}} \cdot \frac{M_0^2}{Q^2 + M_0^2}$$

for fixed W and $\sigma_L = 0$. A good description of the data is found with $M_0^2 = 0.53 \pm 0.04 \pm 0.10 \text{ GeV}^2$. Regge theory then determines the W dependence of the data, combined with lower energy photoproduction experiments, as

$$\sigma_{\text{tot}}^{\gamma p}(W^2) = A_R(W^2)^{\alpha_R - 1} + A_P(W^2)^{\alpha_P - 1}$$

where the Reggeon intercept α_R is fixed to 0.5 from hadroproduction data and lower energy photoproduction data also constrain A_P , A_R and α_P . From the BPC data alone, the pomeron intercept value is

$$\alpha_P^{BPC} = 1.141 \pm 0.020(\text{stat.}) \pm 0.044(\text{sys.})$$

to be compared with the Donnachie-Landshoff value $\alpha_P = 1.08$. In this Q^2 range, the rise of the cross-section is therefore relatively modest. Combining the GVMD and Regge approaches, the resulting ZEUSREGGE fit is used to parameterise the Q^2 and W dependence of the low $Q^2 < 1 \text{ GeV}^2$ data. The ZEUS NLO QCD fit to the ZEUS 94 and ZEUS SVX data, incorporating NMC and BCDMS data, (discussed below) is used to determine the behaviour and the uncertainties on the gluon and singlet quark densities at low x for $Q^2 > 1 \text{ GeV}^2$.

To quantify the behaviour of F_2 , fits to the E665 and ZEUS data of the form $F_2 = c \cdot x^{-\lambda_{\text{eff}}} |_{Q^2}$ are performed. The parameter $\lambda_{\text{eff}} \simeq \alpha_P - 1$ for $x < 0.01$ is then plotted as a function of Q^2 in Fig. 19. A relatively slow transition from $\lambda_{\text{eff}} \simeq 0.1$ is observed with increasing Q^2 . Also shown are fits to the DL and ZEUSREGGE parameterisations, fitted over the same x range as the data, for $Q^2 < 1 \text{ GeV}^2$. These describe the data reasonably but are systematically lower. For $Q^2 > 1 \text{ GeV}^2$, the data are compared to the GRV94 prediction where the starting scale for the evolution of the parton densities is rather low ($\sim 0.3 \text{ GeV}^2$) and pQCD evolution generates the rise at small x : this approach is observed to reasonably describe the data and the description is improved using the GRV98 PDF (not shown). [8] The rise at small x is also described by the ZEUSQCD fit, where the ZEUS data is used as an input.

This rise of F_2 with decreasing x is intimately coupled to the scaling violations via the gluon density (in leading order $dF_2/d \ln Q^2 \sim xg(x)$ neglecting sea quark contributions). In Fig. 20, fits of the form $F_2 = a + b \cdot \ln(Q^2)|_x$ have been performed to the ZEUS data and the parameterisations discussed above. For $x \sim 2 \cdot 10^{-4}$, corresponding to $Q^2 \gtrsim 4 \text{ GeV}^2$ there is a qualitative change in behaviour where the scaling violations stabilise and then decrease for lower- x values, a behaviour which is not reproduced by the GRV94 PDF. The question is whether this scaling violation behaviour and the slow onset of the rise of F_2 with decreasing x can be simultaneously understood.

A. Mueller has discussed the scaling violation behaviour in terms of a geometric model where the spatial extent, R_0 , of the $q\bar{q}$ fluctuation of the virtual photon in the γ^*p fixed-target frame is related to the height of the plateau in the scaling violations [43]

$$\left. \frac{dF_2}{d \ln Q^2} \right|_x \simeq \frac{Q^2(\pi R_0^2)}{4\pi\alpha}.$$

For $\left. \frac{dF_2}{d \ln Q^2} \right|_x \simeq 0.4 \text{ GeV}^{-2}$ and $Q^2 \simeq 4 \text{ GeV}^2$, the spatial extent $R_0 \simeq 0.3 \text{ fm}$. This appears to be the scale at which a transition takes place and the partons in the proton start to overlap. [3] However, perturbative QCD is pushed to its limit and it will be important to test that the parton densities extracted from F_2 can be universally applied.

The ZEUS NLO fit to the $Q^2 > 1 \text{ GeV}^2$ data describes the data, demonstrating that there is sufficient flexibility in such an approach to go down to relatively low Q^2 . However, the relatively stable scaling violations observed around $\langle Q^2 \rangle \sim 4 \text{ GeV}^2$ in Fig. 20 yield a gluon contribution which is rapidly diminishing at small- x and which is in fact smaller than the singlet sea quark contribution for small starting scales. For larger Q^2 values the gluon dominates the sea and we have an intuitively appealing picture where gluons radiate sea quarks whereas, in this low- Q^2 region, the sea appears to be driving the gluon at low x . Whether such low- Q^2 partons are universally valid could be tested using e.g. low- Q^2 diffractive vector meson data. [6, 43]

An important part of the ZEUS NLO QCD fit is the determination of the uncertainties on the gluon and singlet quark densities. These are given for the gluon distribution in Fig. 21. The overall uncertainty is estimated by combining in quadrature: the experimental systematic uncertainties on the ZEUS as well as the NMC and BCDMS data; the theoretical uncertainties on $\alpha_s(M_Z^2)$ by ± 0.005 , the relative strange quark content by $\pm 50\%$ and the charm mass by $\pm 0.2 \text{ GeV}$; and, the parameterisation uncertainties on the starting scale, by varying $1 < Q_0^2 < 7 \text{ GeV}^2$, as well as using a more flexible form of the input in terms of Chebycheff polynomials and redefining the χ^2 including *stat.* \oplus *sys.* errors. These variations correspond to a precision on the gluon of $\sim 10\%$ at $Q^2 = 20 \text{ GeV}^2$ where the renormalisation and factorisation scales are set to $\mu_R^2 = \mu_F^2 = Q^2$. The role of the scale uncertainties is discussed in [44] with respect to future capabilities to determine $\alpha_s(M_Z^2)$ at HERA. The theoretical and parameterisation uncertainties are amplified at low Q^2 such that the gluon is rather poorly determined from the scaling violations of F_2 in the transition region discussed above.⁴⁾ It is clear, however, that the gluon is significantly suppressed at low Q^2 .

F₂^c Determination: $D^* \rightarrow (K\pi)\pi_s$ measurements in DIS provide a significant test of the gluon density of the proton determined from the scaling violations of F_2 . They also help to constrain theoretical uncertainties in the fits to F_2 where different prescriptions for charm production are adopted. The ZEUS preliminary cross-section $\sigma^{ep \rightarrow D^{*X}} = 8.55 \pm 0.31_{-0.50}^{+0.30} \text{ nb}$ is measured in the range $1 < Q^2 < 600 \text{ GeV}^2$, $0.02 < y < 0.7$, $1.5 < p_T^{D^*} < 15 \text{ GeV}$, and $|\eta^{D^*}| < 1.5$. In general, the H1 [45] and ZEUS [46] data agree with the Harris-Smith NLO calculations [47] where the fraction $f(c \rightarrow D^{*+}) = 0.222 \pm 0.014 \pm 0.014$ is determined from LEP data [48], the Peterson fragmentation function is characterised by $\epsilon_c = 0.035$ and the renormalisation and factorisation

⁴⁾ The gluon can even become negative at low Q^2 (in $\overline{\text{MS}}$ scheme) but the physical quantities, F_2 , F_2^c and F_L remain positive within the quoted errors.

scales are set to $\mu_R^2 = \mu_F^2 = Q^2 + 4m_c^2$. There is, however, a small discrepancy at lower x_{D^*} and higher η^{D^*} , corresponding to the proton direction, where the data lie above the prediction. A similar discrepancy is also observed in the first analysis in the semi-leptonic decay channel. [46] Together these results indicate that the fragmentation of charm in ep processes is worthy of further investigation. At this stage, it is reasonable to extrapolate the measured cross-section to the full $\{\eta, p_T\}$ range⁵⁾ to determine $F_2^c(x, Q^2)$ via the expression

$$\frac{d^2\sigma_{c\bar{c}X}}{dx dQ^2} = \frac{2\pi\alpha^2}{xQ^4} [Y_+ F_2^c(x, Q^2) - y^2 F_L^c(x, Q^2)]$$

where the F_L^c contribution can be estimated as a QCD correction. In Fig. 22, the HERA $F_2^c(x, Q^2)$ data mirror the rise of F_2 at small x . The data are in agreement with the GRV94 PDF, where the band represents an estimated theoretical uncertainty due to the effective charm mass ($m_c = 1.4 \pm 0.2$ GeV). This comparison verifies the steep rise of the gluon density at low x with a precision of $\simeq 15 - 20\%$.

F_L Determination: The contribution of F_L enters as a QCD correction to the total DIS cross-section where $F_L = F_2 - 2xF_1$. As such it provides an additional method to calibrate the gluon at low x . H1 [42] have used two methods to extract F_L from the reduced cross-section $\tilde{\sigma} = F_2 - \frac{y^2}{Y_+} \cdot F_L$ at high y . This is the region where the scattered electron energy is low: in the H1 analysis scattered positrons are measured down to $E_{e'} > 3$ GeV and backgrounds reduced by requiring the associated track to have correct charge. F_L is determined as a function of $Q^2 \geq 3$ GeV² by measuring local derivatives of $\partial\tilde{\sigma}/\partial \log y$ and observing deviations from a straight line at high y . These data are denoted by the stars in Fig. 23. Here, the data are compared to an earlier extrapolation method [49] applied to the same data, which yields consistent results, as well as to the H1 NLO QCD fit to H1, NMC and BCDMS F_2 data. The data are in agreement with the QCD expectations although there is an indication of a relatively large F_L contribution at the highest y (corresponding to lowest x) values. In conclusion, a consistent value for the gluon density at low $x \lesssim 10^{-2}$ may be extracted from the data on F_2 , F_2^c and F_L with a precision of $\sim 10\%$ at $Q^2 = 20$ GeV².

4.2 High- Q^2 Cross-Sections

The HERA collider provides a unique window to explore ep interactions at the highest energies, extending the range of momentum transfer Q^2 by about two orders of magnitude compared to fixed-target experiments. As the HERA luminosity increases we explore the region of $Q^2 \sim 10^4$ GeV², where electroweak effects play a rôle. It is in this unexplored kinematic region that we are sensitive to deviations from the standard model (SM).

In 1997, H1 [50] and ZEUS [51] reported an excess of events compared to the SM predictions from the neutral current (NC) data taken during 1994 to 1996. For the H1 analysis an accumulation of 7 events in a reconstructed e^+q mass window of 200 ± 12 GeV was found, compared to an expectation of 0.95 ± 0.18 from 15 pb^{-1} of data. One further event was found from the

⁵⁾This procedure neglects the possibility of additional contributions outside the measured region due, for example, to intrinsic charm.

1997 data corresponding to a further 22 pb^{-1} , yielding 8 events compared to an expectation of 3.01 ± 0.54 . For the ZEUS analysis the observed rates agreed with expectations except for an excess at the highest Q^2 where two outstanding events with $Q^2 \simeq 40,000 \text{ GeV}^2$ were observed from a luminosity of 20 pb^{-1} . These events still clearly stand out but no new NC outstanding events are observed in the 1997 data, corresponding to a further 26.5 pb^{-1} . Similarly in the charged current (CC) channel, the number of events is higher than expectations but is consistent with the standard model. Attention has therefore focussed on measuring the cross-sections at the highest accessible Q^2 values.

The theoretical uncertainty on the cross-sections was determined as discussed w.r.t. the ZEUS low- Q^2 NLO QCD fit using high- x F_2^p and F_2^n data to yield SM cross-section uncertainties of $\simeq 6\text{-}8\%$ on the NC cross-section and $\simeq 6\text{-}12\%$ on the CC cross-section at the highest accessible Q^2 values. These cross-sections therefore represent a benchmark for the standard model. The cross-sections, discussed below, are corrected to the electroweak Born level and integrated over the measured range of y for H1 [52] and corrected to the complete y range for ZEUS. [53]

Neutral Current Cross-Sections: High- Q^2 neutral current events are easily identified from the high-energy scattered positron. The cross-section is particularly sensitive to the valence u -quark distribution in the proton

$$\frac{d^2\sigma_{e+p}}{dx dQ^2} \simeq \frac{2\pi\alpha^2}{xQ^4} [Y_+ F_2(x, Q^2) - Y_- xF_3(x, Q^2)].$$

Here, F_2 is the generalised structure function, incorporating γ and Z terms, which is sensitive to the singlet sum of the quark distributions ($xq + x\bar{q}$) and xF_3 is the parity-violating (Z -contribution) term which is sensitive to the non-singlet difference of the quark distributions ($xq - x\bar{q}$). The data are now becoming sensitive to electroweak γZ interference effects, which suppress the NC cross-section by $\sim 30\%$ for $Q^2 > 10,000 \text{ GeV}^2$. [52, 53]

In the upper plot of Fig. 24, the H1 cross-section is observed to fall over more than six orders of magnitude. The ratio of the data to the SM, adopting the H1 NLO QCD fit, is shown in the lower plot of Fig. 24 where agreement is observed up to $Q^2 \simeq 30,000 \text{ GeV}^2$. Comparison of the the data uncertainties with those from theory (not shown) indicates that the data will constrain the parton densities of the proton at large x .

Charged Current Cross-Sections: Charged current events are identified by their missing transverse momentum (p_T) due to the escaping neutrino. The cross-section is sensitive to the valence d -quark distribution in the proton

$$\frac{d^2\sigma_{e+p}}{dx dQ^2} \simeq \frac{G_F^2}{2\pi} \left(\frac{M_W^2}{Q^2 + M_W^2} \right)^2 [\bar{u} + \bar{c} + (1-y)^2(d+s)].$$

In the ZEUS analysis, $d\sigma^{CC}/dQ^2$ was measured for $Q^2 > 400 \text{ GeV}^2$ using the Jacquet-Blondel method where $Q_{JB}^2 = p_T^2/1-y_{JB}$, with an RMS resolution on $Q^2 \simeq 25\%$, reflecting the $35\%/\sqrt{E}$ hadronic energy resolution. The systematic uncertainties, mainly due to the hadronic energy scale uncertainty of $\pm 3\%$, correspond to $\sim 15\%$ uncertainties on the cross-section at lower Q^2 but increase at larger x and Q^2 .

In the upper plot of Fig. 25 the cross-section is observed to fall over more than four orders of magnitude. The ratio of the data to the SM, adopting the CTEQ4D PDF, is shown in the lower plot of Fig. 25 where good agreement is observed up to Q^2 of $\simeq 10,000 \text{ GeV}^2$. Comparison of the the data uncertainties with those from theory (shaded band) indicates that the data will help to constrain the d -quark densities at large- x . The cross-section is suppressed relative to NC γ exchange due to the propagator term: this characteristic dependence on Q^2 has been fitted to yield a value for the mass of the exchanged (space-like) W -boson of

$$M_W = 78.6_{-2.4}^{+2.5}(\text{stat.})_{-3.0}^{+3.3}(\text{sys.}) \text{ GeV} \quad (\text{ZEUS prelim.})$$

$$M_W = 81.2 \pm 3.3(\text{stat.}) \pm 4.3(\text{sys.}) \text{ GeV} \quad (\text{H1 prelim.})$$

with an additional PDF uncertainty of $\pm 1.5 \text{ GeV}$ estimated in the ZEUS analysis and an uncertainty of $\pm 3 \text{ GeV}$ due to electroweak radiative corrections estimated in the H1 analysis.

Returning to the Bodek-Yang analysis, [19] discussed in relation to the fixed-target results, the ZEUS CC cross-section is plotted as function of x for $Q^2 > 400 \text{ GeV}^2$ in Fig. 26. The increase in the ratio of d/u corresponds to an increase of the CC cross-section at high x . The uncertainties on the data are large in this region, but this modification does result in better agreement with the data than the standard PDF's at large x .

A comparison of the H1 and ZEUS NC and CC cross-sections for $Q^2 > 1000 \text{ GeV}^2$ is given in Fig. 27. The NC and CC data are in agreement and both cross-sections agree with the SM prediction over a broad range range of Q^2 . At high $Q^2 > 10,000 \text{ GeV}^2$, the CC cross-section is suppressed relative to the NC cross-section due to the d/u ratio being less than unity. The measurement of the HERA CC/NC ratio of cross-sections will therefore provide a direct determination of this ratio, free from the uncertainties due to nuclear binding effects.

5 Summary and Outlook

There were many highlights in our deepening understanding of nucleon structure presented at the ICHEP98 conference. CCFR have performed final analyses of their structure function data which lead to precise tests of QCD. NuTeV already provide electroweak input and aim to reduce the uncertainty on $\alpha_s(M_Z^2)$ to ± 0.002 . Important developments have been made in the understanding of higher twist effects in terms of renormalon theory. Input from various experiments and a reassessment of the importance of nuclear binding effects in the deuteron lead to the conclusion that the ratio of d/u parton densities increases, whilst the ratio of \bar{d}/\bar{u} decreases compared to earlier determinations.

The second phase of spin experiments are now exploring spin structure via NLO QCD fits. The first observations of scaling violations from combined fits to the world data indicate that the source of the spin puzzle lies with the gluon spin density, Δg , although large uncertainties remain. Semi-inclusive measurements now provide input on the quark composition of the spin.

The first discovery at HERA was the rise of F_2 at low x . Precise data now enable the rise of the associated scaling violations with decreasing x and hence the gluon to be determined. The

determinations of F_2^c and F_L enable this gluon distribution to be calibrated. The fall of these scaling violations at low (x, Q^2) enables the region where parton confinement effects take place to be explored at high energies.

The large e^+p data sample enables cross-sections to be measured at very large Q^2 where electroweak effects start to play a rôle. The HERA data are consistent with the Standard Model and place constraints on the parton densities at large x . The outlook is for a similar sample of $\sim 50\text{pb}^{-1}$ of e^-p data in the next two years, prior to the HERA upgrade where luminosities will be increased five-fold. Deep inelastic scattering has historically led to the discovery of the nucleus, quarks and electroweak neutral currents. The discovery potential of current and future experiments is high and the field continues to provide important input to our understanding of sub-nuclear structure.

Acknowledgements

It is a pleasure to thank Alan Astbury and co-organisers for an excellent conference. Many thanks to Halina Abramowicz, Arie Bodek, Antje Brull, Allen Caldwell, Abe Deshpande, John Dainton, Robin Devenish, Martin Erdmann, Laurent Favart, Thomas Gehrmann, Tim Greenshaw, Beate Heinemann, Peppe Iacobucci, Robert Klanner, Max Klein, Masahiro Kuze, Ludger Lindemann, Alan Martin, Gavin McCance, Jan Okrasinski, Jen-Chieh Peng, Alex Prinias, Robert Waugh, Arnulf Quadt, David Saxon, Stefan Schlenstedt, Mike Vetterli, Manuella Vinciter, Bryan Webber, Jim Whitmore, Un-Ki Yang, Rik Yoshida, Jaehoon Yu and all the speakers in the structure functions parallel session for their help, inspiration and advice. I am grateful to the Alexander von Humboldt Foundation, DESY and PPARC for their financial support.

References

- [1] V. Fadin and L. Lipatov, hep-ph/9802290.
- [2] J.R. Forshaw, G.P. Salam and R.S. Thorne, hep-ph/9812304.
- [3] L.V. Gribov, E.M. Levin and M.G. Ryskin, *Phys. Rep.* **100**, 1 (1983); E.M. Levin and M.G. Ryskin, *Nucl. Phys. B* **18C**, 92 (1990).
- [4] J. Huston, ICHEP98 proceedings.
- [5] Y. Dokshitzer, ICHEP98 proceedings.
- [6] M. Erdmann, ICHEP98 proceedings.
- [7] A.D. Martin, R.G. Roberts, W.J. Stirling and R.S. Thorne, hep-ph/9803445.
- [8] M. Glück, E. Reya and A. Vogt, hep-p/9806404.
- [9] CTEQ Collab., H.L. Lai et al., *Phys. Rev. D* **55**, 1280 (1997).

- [10] S.A. Larin and J.A.M. Vermaseren, *Phys. Lett. B* **259**, 345 (1991).
- [11] A.L. Kataev and V.V. Starshenko, *Mod. Phys. Lett. A* **10**, 235 (1991).
- [12] J.H. Kim, D.A. Harris et al., hep-ex/9808015, submitted to *Phys. Rev. Lett.*.
- [13] S.A. Kulagin, hep-ph/9809219.
- [14] A.L. Kataev, G. Parente and A.V. Sidorov, hep-ph/9809500.
- [15] CCFR Collab., W. Seligman et al., hep-ph/9701017.
- [16] M. Virchaux and A.M. Milsztajn, *Phys. Lett. B* **274**, 221 (1992).
- [17] C. Caso et al., *Euro. Phys. C* **3**, 1 (1998).
- [18] F. Eisele, Physics in Collision proceedings, hep-ph/9807028.
- [19] U. Yang and A. Bodek, ICHEP98 proceedings, hep-ph/9809480.
- [20] L. Frankfurt and M. Strikman, *Phys. Rep.* **160**, 235 (1988).
- [21] M. Dasgupta and B.R. Webber, *Phys. Lett. B* **382**, 273 (1996).
- [22] CCFR Collab., U.K. Yang et al., DIS98 proceedings, hep-ex/9806023; J. Yu, ICHEP98 proceedings.
- [23] CDF Collaboration, F. Abe et al., hep-ex/9809001, submitted to *Phys. Rev. Lett.*; W. Sakumoto, ICHEP98 proceedings.
- [24] NMC Collab., M. Arneodo et al., *Phys. Rev. D* **50**, 1 (1994).
- [25] S. Kumano and K. Umekawa, hep-ph/9803359.
- [26] E866 Collab., E.A. Hawker et al., *Phys. Rev. Lett.* **80**, 3715 (1998).
- [27] E866 Collab., J.C. Peng et al., hep-ex 9804288, submitted to *Phys. Rev. D*.
- [28] HERMES Collab., K. Ackerstaff et al., hep-ex/9807013; M. Vinciter, ICHEP98 proceedings.
- [29] C. Boros, J. Londergan and A. Thomas, hep-ph/9804410. C. Boros, ICHEP98 proceedings.
- [30] CCFR Collab., A. Bazarko et al., *Z. Phys. C* **65**, 189 (1995).
- [31] D. Karlen, ICHEP98 proceedings.
- [32] SMC Collab., B. Adeva et al., CERN-EP/98-86, submitted to *Phys. Rev. D*; A. Deshpande, ICHEP98 proceedings.
- [33] G. Altarelli, R.D. Ball, S. Forte and G. Ridolfi, *Nucl. Phys. B* **496**, 337 (1997).
- [34] L. Sorrell, ICHEP98 proceedings.

- [35] E. Rondio, ICHEP98 proceedings.
- [36] F.E. Close and R.G. Roberts, *Phys. Lett. B* **336**, 1257 (1994).
- [37] J. Ellis, DIS98 proceedings (World Scientific) in press; J. Ellis and M. Karliner, *Phys. Lett. B* **341**, 397 (1995).
- [38] B. Lampe and E. Reya, hep-ph/9810270.
- [39] SMC Collab., D. Adeva et al., hep-ex/9711008, submitted to *Phys. Lett. B*.
- [40] C.A. Miller, ICHEP98 proceedings.
- [41] ZEUS Collab., J. Breitweg et al., DESY 98-121, submitted to *Euro. Phys. C*; A. Quadt, ICHEP98 proceedings.
- [42] H1 Collab., C. Adloff et al., ICHEP98 contributed papers 534 and 535; M. Klein, ICHEP98 proceedings.
- [43] A.H. Mueller, DIS98 proceedings (World Scientific) in press.
- [44] M. Botje, DIS97 proceedings, *AIP Conf. Proc.* **407**, 393 (1997).
- [45] H1 Collab., C. Adloff et al., ICHEP98 contributed papers 538 and 540; E. Tzamariudaki, ICHEP98 proceedings.
- [46] ZEUS Collab., J. Breitweg et al., ICHEP98 contributed papers 768 and 772; W. Verkerke, ICHEP98 proceedings.
- [47] B.W. Harris and J. Smith, *Nucl. Phys. B* **452**, 109 (1995); B.W. Harris and J. Smith, *Phys. Lett. B* **353**, 535 (1995); B.W. Harris and J. Smith, hep-ph/9706334.
- [48] OPAL Collab., K. Ackerstaff et al., *Euro. Phys. C* **1**, 439 (1998).
- [49] H1 Collab., S. Aid et al., *Phys. Lett. B* **393**, 452 (1997).
- [50] H1 Collab., C. Adloff et al., *Z. Phys. C* **74**, 191 (1997).
- [51] ZEUS Collab., J. Breitweg et al., *Z. Phys. C* **74**, 207 (1997).
- [52] H1 Collab., C. Adloff et al., ICHEP98 contributed paper 533; M. Fleischer, ICHEP98 proceedings.
- [53] ZEUS Collab., J. Breitweg et al., ICHEP98 contributed papers 751 and 752; J. Grosse-Knetter, ICHEP98 proceedings.

Table 1: Processes studied in global parton distribution fits. \star indicates new preliminary data presented at ICHEP98, included in this review. \dagger indicates final data presented at ICHEP98. $*$ indicates data used in the MRST fits. (Courtesy of A. Martin.)

Process/ Experiment	Leading order subprocess	Parton behaviour probed
DIS ($\mu N \rightarrow \mu X$) $F_2^{\mu p}, F_2^{\mu d}, F_2^{\mu n} / F_2^{\mu p}$ (SLAC, BCDMS, NMC, E665)*	$\gamma^* q \rightarrow q$	Four structure functions \rightarrow $u + \bar{u}$ $d + \bar{d}$ $\bar{u} + \bar{d}$ s (assumed = \bar{s}), but only $\int xg(x, Q_o^2)dx \simeq 0.35$ and $\int(\bar{d} - \bar{u})dx \simeq 0.1$
DIS ($\nu N \rightarrow \mu X$) $F_2^{\nu N}, xF_3^{\nu N}$ (CCFR)* \dagger	$W^* q \rightarrow q'$	
DIS (small x) F_2^{ep} (H1, ZEUS)* \star	$\gamma^*(Z^*)q \rightarrow q$	λ ($x\bar{q} \sim x^{-\lambda_s}, xg \sim x^{-\lambda_g}$)
DIS (F_L) NMC, HERA \star	$\gamma^* g \rightarrow q\bar{q}$	g
$\ell N \rightarrow c\bar{c}X$ F_2^c (EMC; H1, ZEUS)* \star	$\gamma^* c \rightarrow c$	c ($x \gtrsim 0.01; x \lesssim 0.01$)
$\nu N \rightarrow \mu^+ \mu^- X$ (CCFR)*	$W^* s \rightarrow c$ $\hookrightarrow \mu^+$	$s \approx \frac{1}{4}(\bar{u} + \bar{d})$
$pN \rightarrow \gamma X$ (WA70*, UA6, E706, ...)	$qg \rightarrow \gamma q$	g at $x \simeq 2p_T/\sqrt{s} \rightarrow$ $x \approx 0.2 - 0.6$
$pN \rightarrow \mu^+ \mu^- X$ (E605, E772)*	$q\bar{q} \rightarrow \gamma^*$	$\bar{q} = \dots(1-x)^{\eta_s}$
$pp, pn \rightarrow \mu^+ \mu^- X$ (E866, NA51)* \dagger	$u\bar{u}, d\bar{d} \rightarrow \gamma^*$ $u\bar{d}, d\bar{u} \rightarrow \gamma^*$	$\bar{u} - \bar{d}$ ($0.04 \lesssim x \lesssim 0.3$)
$ep, en \rightarrow e\pi X$ (HERMES) \dagger	$\gamma^* q \rightarrow q$ with $q = u, d, \bar{u}, \bar{d}$	$\bar{u} - \bar{d}$ ($0.04 \lesssim x \lesssim 0.2$)
$p\bar{p} \rightarrow WX(ZX)$ (UA1, UA2; CDF, D0) $\rightarrow \ell^\pm$ asym (CDF)* \dagger	$ud \rightarrow W$	u, d at $x \simeq M_W/\sqrt{s} \rightarrow$ $x \approx 0.13; 0.05$ slope of u/d at $x \approx 0.05 - 0.1$
$p\bar{p} \rightarrow t\bar{t}X$ (CDF, D0)	$q\bar{q}, gg \rightarrow t\bar{t}$	q, g at $x \gtrsim 2m_t/\sqrt{s} \simeq 0.2$
$p\bar{p} \rightarrow \text{jet} + X$ (CDF, D0)	$gg, qg, qq \rightarrow 2j$	q, g at $x \simeq 2E_T/\sqrt{s} \rightarrow$ $x \approx 0.05 - 0.5$

Table 2: Processes studied in global spin parton distribution fits. The first group of datasets correspond to current experiments. The second group correspond to near-future (year 2000) experiments. The third group correspond to potential year 2005 experiments at HERA. (Courtesy of T. Gehrmann.)

Process/ Experiment	Leading order subprocess	Parton behaviour probed
DIS ($\ell N \rightarrow \ell X$) $g_1^{\ell p}, g_1^{\ell d}, g_1^{\ell n}$ (SLAC, EMC/SMC, HERMES)	$\gamma^* q \rightarrow q$	Two structure functions \rightarrow $\sum_q e_q^2 (\Delta q + \Delta \bar{q})$ $\Delta A_3 = \Delta u + \Delta \bar{u} - \Delta d - \Delta \bar{d}$
$\ell p, \ell n \rightarrow \ell \pi X$ (SMC, HERMES)	$\gamma^* q \rightarrow q$ with $q = u, d, \bar{u}, \bar{d}$	$\Delta u_v, \Delta d_v, \Delta \bar{q}$
$\ell N \rightarrow c \bar{c} X$ (COMPASS, HERMES)	$\gamma g \rightarrow c \bar{c}$	Δg $(x \approx 0.15, 0.3)$
$\ell N \rightarrow h^+ h^- X$ (COMPASS)	$\gamma g \rightarrow q \bar{q}$ $\gamma q \rightarrow qg$	Δg $(x \approx 0.1)$
$pp \rightarrow (\gamma^*, W^\pm, Z^0) X$ (RHIC)	$q \bar{q} \rightarrow \gamma^*, W^\pm, Z^0$	$\Delta u, \Delta \bar{u}, \Delta d, \Delta \bar{d}$ $(x \gtrsim 0.06)$
$pp \rightarrow \text{jets } X$ (RHIC)	$q \bar{q}, qq, qg, gg \rightarrow 2j$	Δg (?) $(x \gtrsim 0.03)$
$pp \rightarrow \gamma X$ (RHIC)	$qg \rightarrow q\gamma$ $q \bar{q} \rightarrow g\gamma$	Δg $(x \gtrsim 0.03)$
DIS ($e^\pm p \rightarrow \nu X$) g_1^\pm, g_5^\pm (HERA)	$W^* q \rightarrow q'$	Two structure functions \rightarrow $\Delta u - \Delta \bar{d} - \Delta \bar{s}$ $\Delta d + \Delta s - \Delta \bar{u}$
DIS (small x) g_1^{ep} (HERA)	$\gamma^* q \rightarrow q$	$\alpha_{q,g}$ $(\Delta \bar{q} \sim x^{\alpha_q}, \Delta g \sim x^{\alpha_g})$
$\ell N \rightarrow \ell \text{jets } X$ (HERA)	$\gamma^* g \rightarrow q \bar{q}$ $\gamma^* q \rightarrow qg$	Δg $(x \gtrsim 0.0015)$
$pp \rightarrow \ell^+ \ell^- X$ (HERA-N)	$q \bar{q} \rightarrow \gamma^*$ 35	$\Delta \bar{q}$ $(x \gtrsim 0.15)$

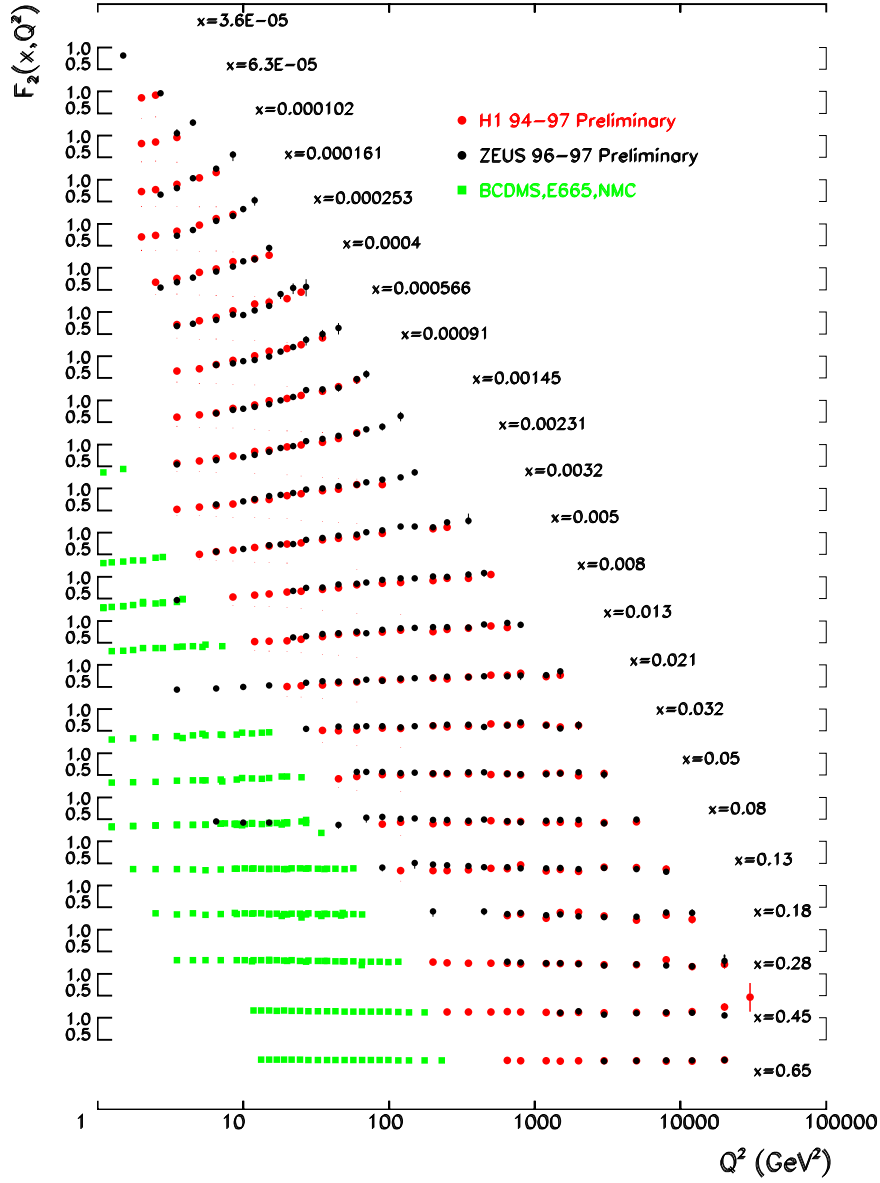


Figure 17: Scaling violations of F_2 versus Q^2 for various x ranges from the latest H1 and ZEUS preliminary data compared to fixed-target experiments. (The quoted x values correspond to the ZEUS measurements or the nearest x values from other experiments).

HERA 1995-1997 preliminary

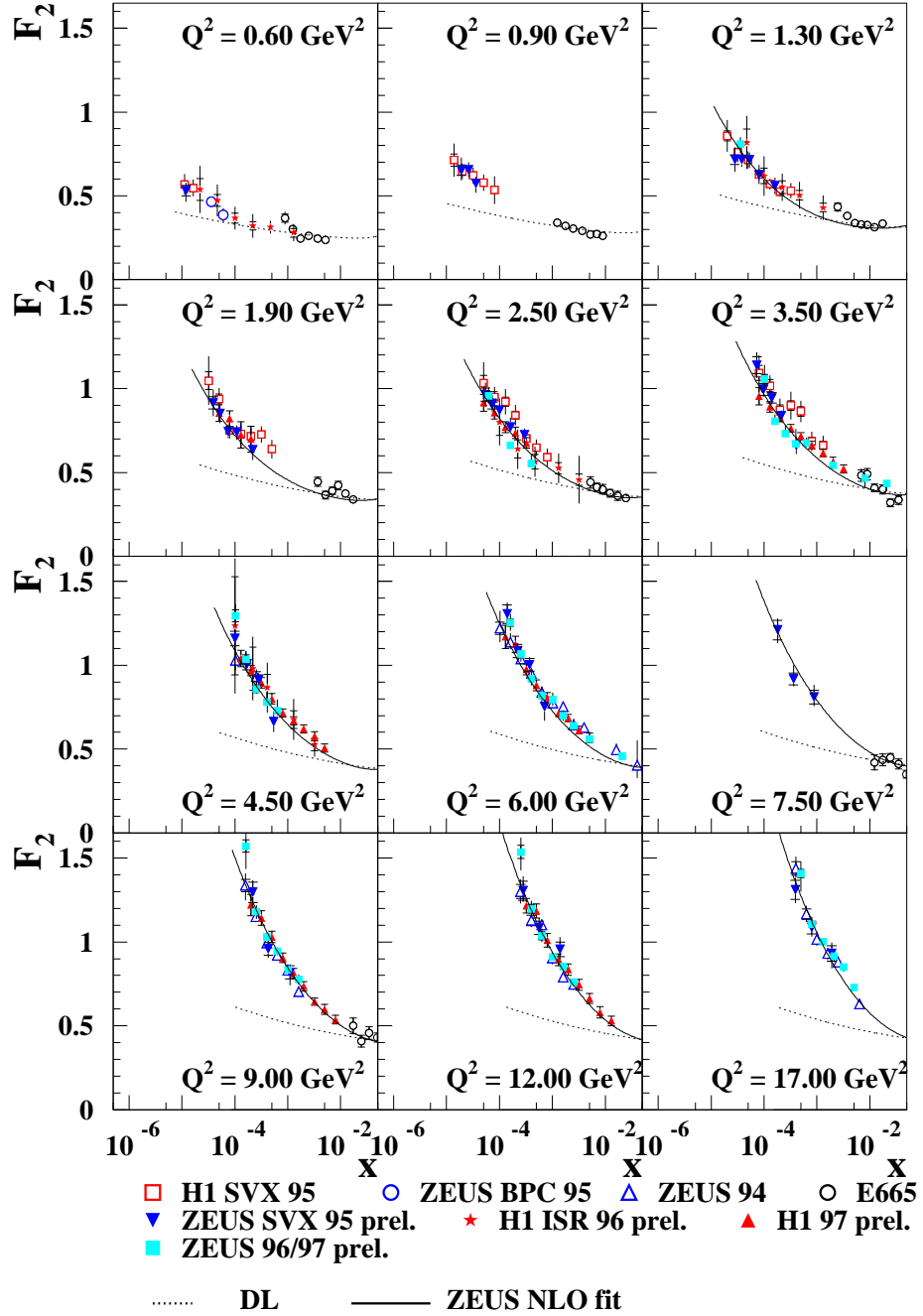


Figure 18: HERA F_2 data for various Q^2 intervals as a function of x exploring the transition region. The data are compared to the Donnachie-Landshoff Regge model (lower dotted line) and the ZEUS NLO QCD fit (full line) discussed in the text.

ZEUS 1995

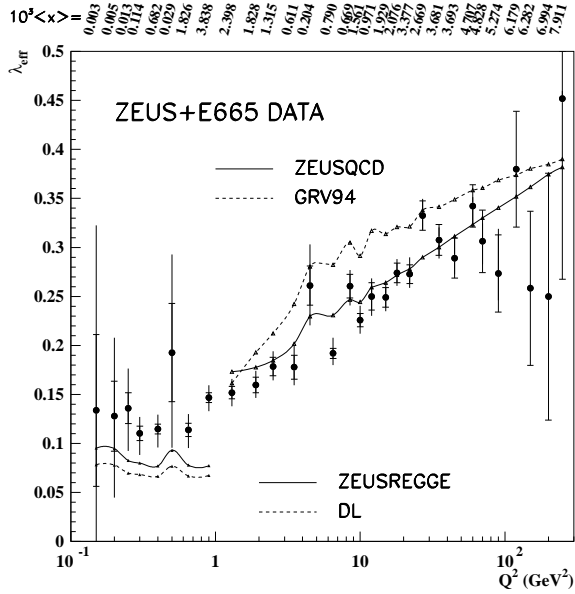


Figure 19: λ_{eff} versus Q^2 and $\langle x \rangle$ from fits to ZEUS and E665 data of the form $F_2 = c \cdot x^{-\lambda_{\text{eff}}} |_{Q^2}$. The data are compared to the QCD and Regge fits discussed in the text.

ZEUS 1995

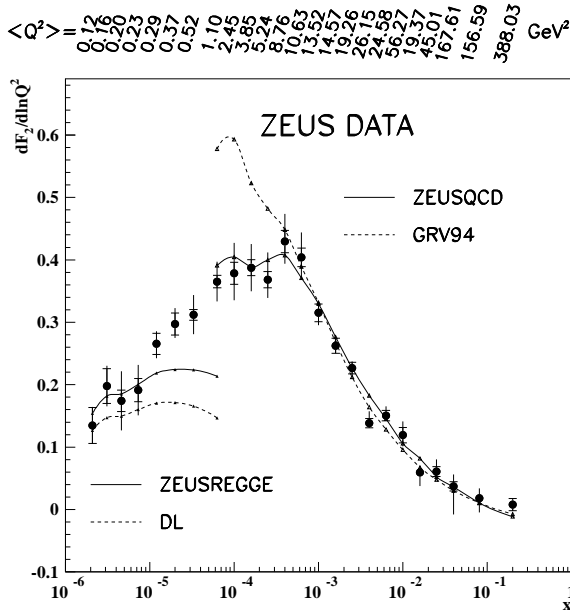


Figure 20: $dF_2/d\ln Q^2$ versus x and $\langle Q^2 \rangle$ from fits to ZEUS data of the form $F_2 = a + b \cdot \ln(Q^2) |_x$. The data are compared to the QCD and Regge fits discussed in the text.

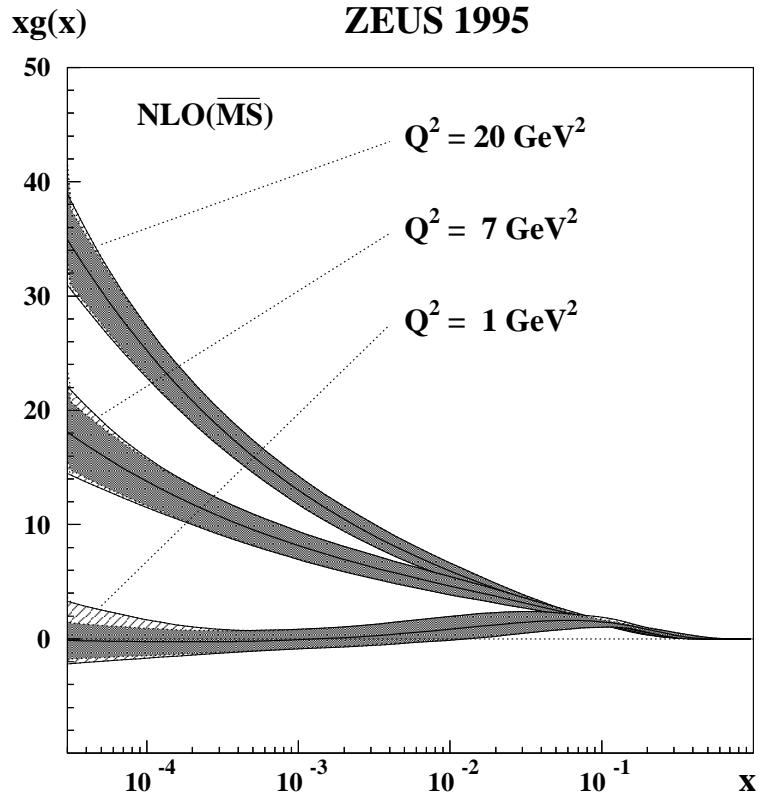


Figure 21: Gluon momentum distribution, $xg(x)$ at $Q^2 = 1, 7$ and 20 GeV^2 in $\overline{\text{MS}}$ scheme including the uncertainties discussed in the text. The shaded band corresponds to the experimental and theoretical uncertainties and the hatched band indicates the parameterisation errors discussed in the text.

HERA 95-97 PRELIMINARY

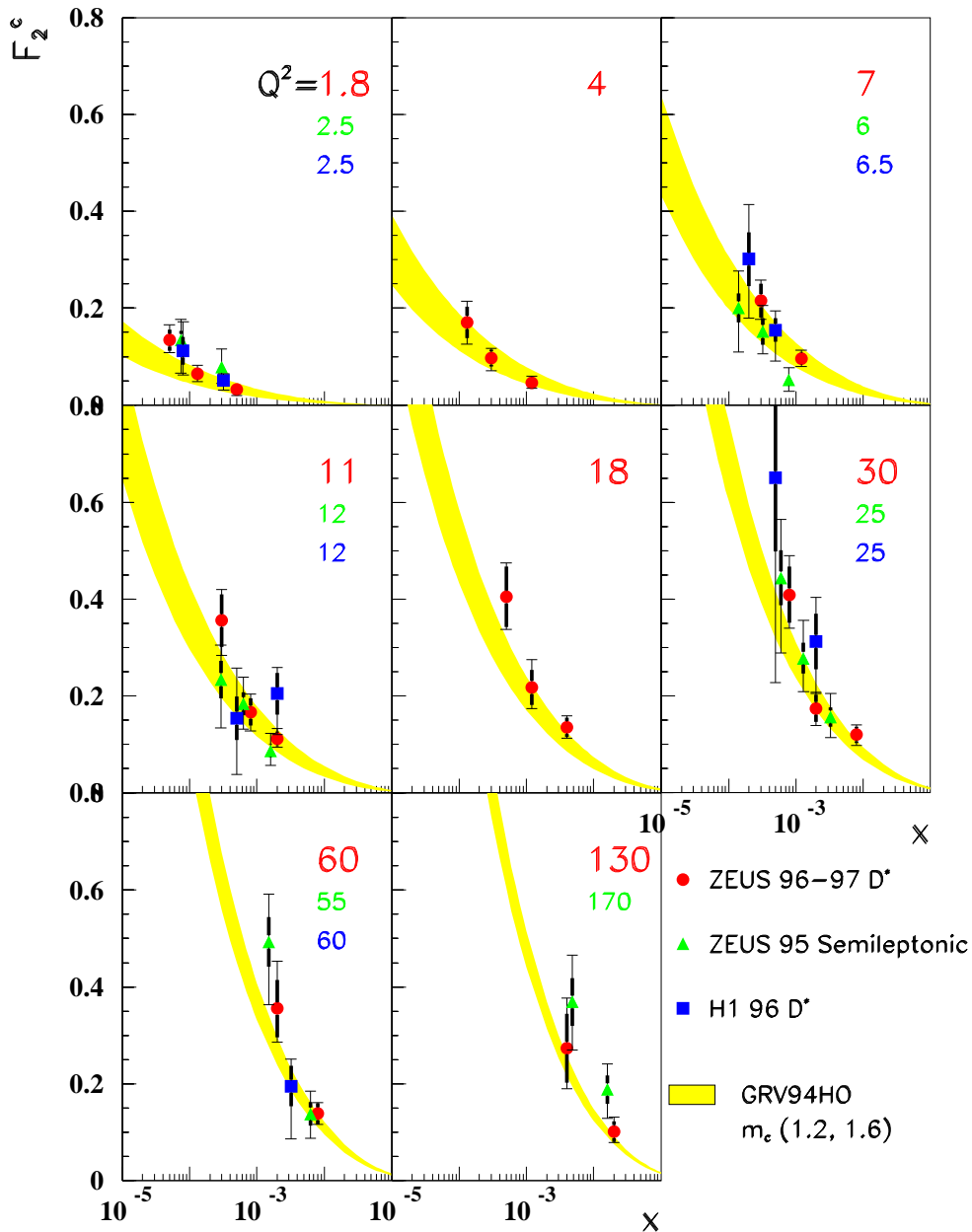


Figure 22: HERA F_2^c data for various Q^2 intervals as a function of x . The data are compared to the Harris-Smith NLO QCD calculation using the GRV94 PDF input discussed in the text.

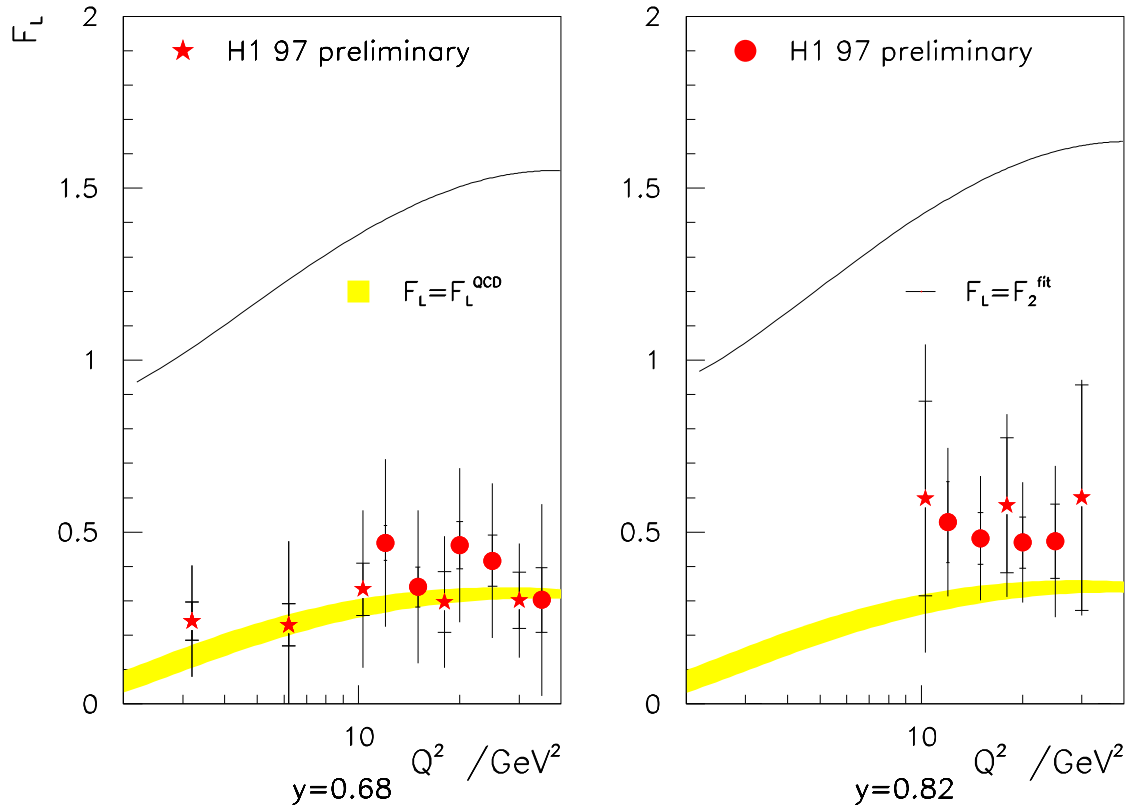


Figure 23: H1 determination of F_L versus Q^2 for $y = 0.68$ and $y = 0.82$ using the derivative method (\star) compared to the published method (\bullet) and the NLO QCD fit expectation (shaded band). The upper limit $F_L = F_2$ is indicated by the full line.

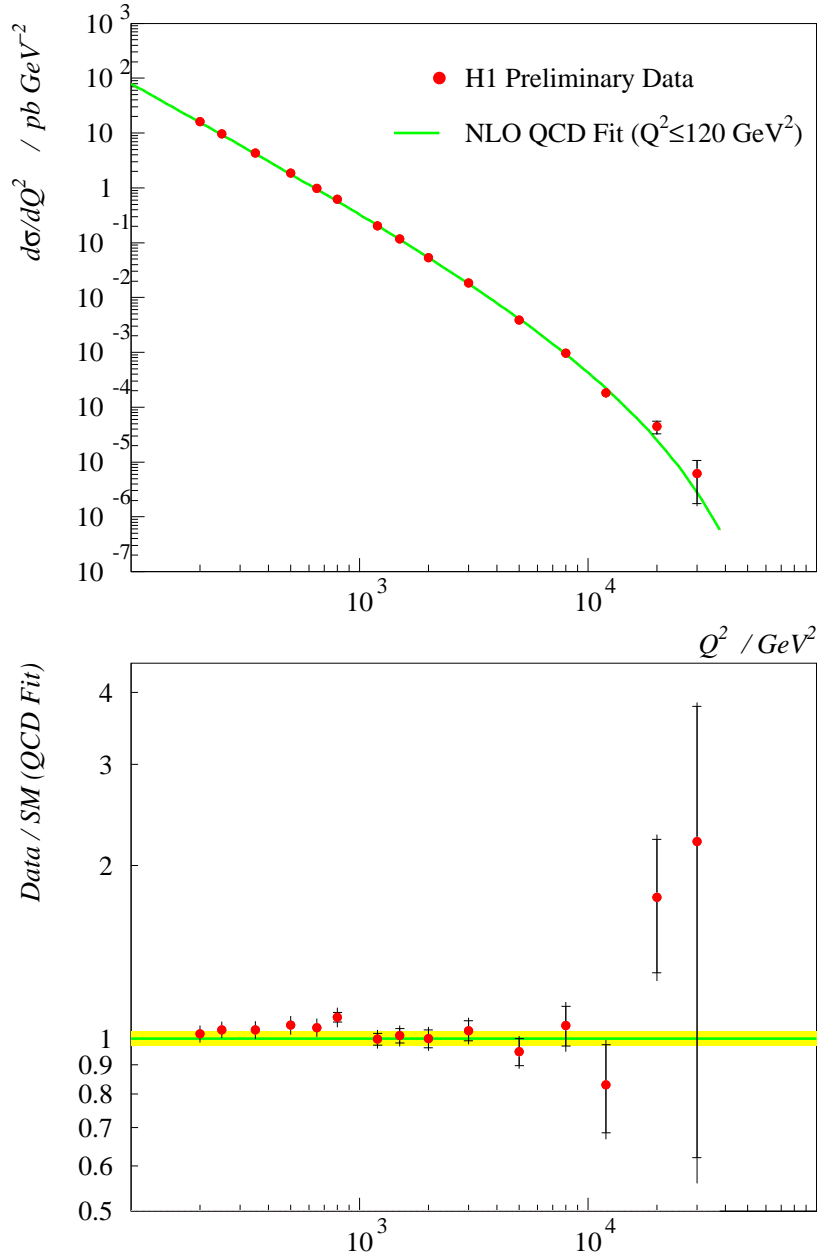


Figure 24: H1 neutral current cross-section $d\sigma^{NC}/dQ^2$ versus Q^2 for $Q^2/\text{GeV}^2 < 0.9$ and $E_{e'} > 11 \text{ GeV}$ (upper plot) and ratio with respect to the standard model prediction (lower plot). The shaded band represents the luminosity uncertainty of $\pm 2.6\%$.

ZEUS Preliminary 1994-97

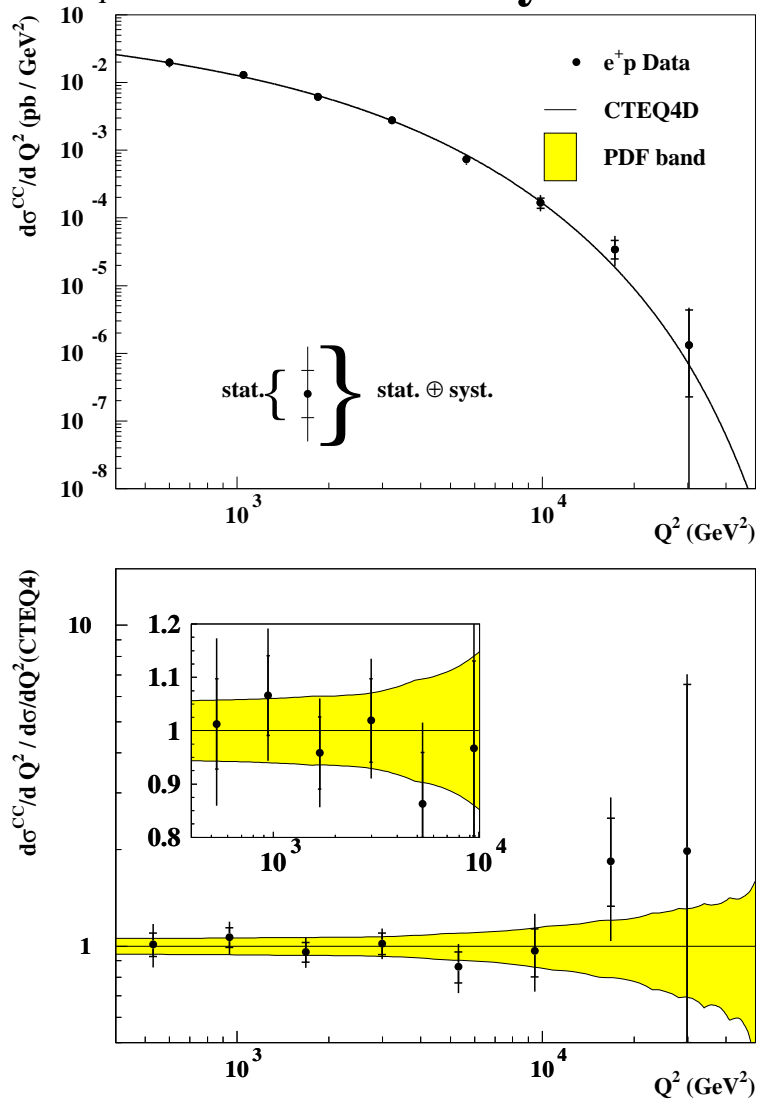


Figure 25: ZEUS charged current cross-section $d\sigma^{CC}/dQ^2$ versus Q^2 for $0 < y < 1$ (upper plot) and ratio with respect to the standard model prediction (lower plot). The shaded band in the ratio plot represents the ZEUS NLO QCD fit uncertainty.

ZEUS CC Preliminary 1994-97

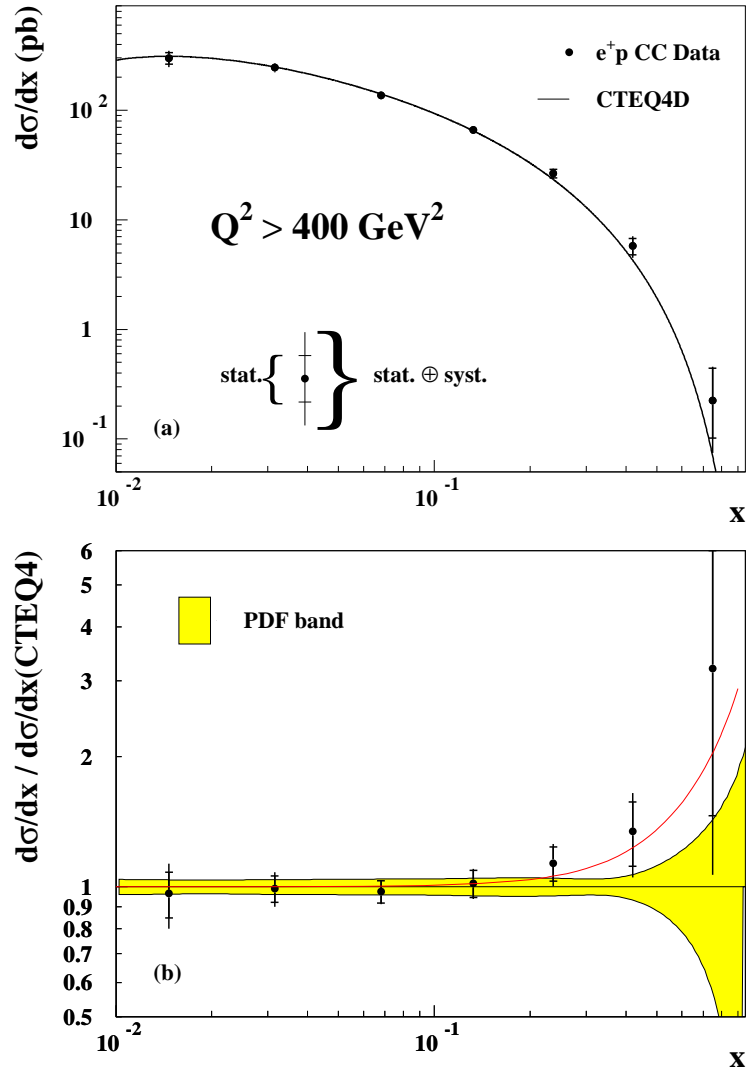


Figure 26: ZEUS charged current cross-section $d\sigma^{CC}/dx$ versus x for $Q^2 > 400 \text{ GeV}^2$ and ratio with respect to the standard model prediction (lower plot). The upper curve in the ratio plot represents the Bodek-Yang d/u modified MRS(R2) parameterisation discussed in the text.

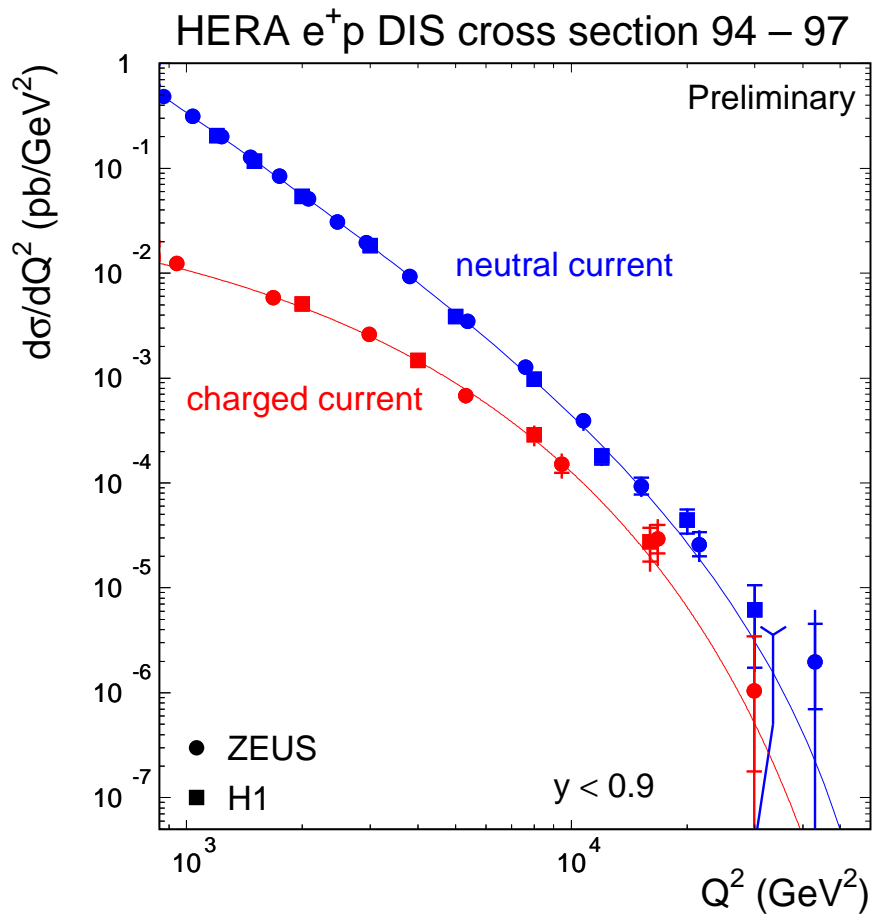


Figure 27: HERA e^+p DIS cross-sections neutral and charged current data for $y < 0.9$ compared to the standard model prediction, adopting the CTEQ4D PDF.